GOME-2A retrievals of tropospheric NO_2 in different spectral ranges - influence of penetration depth

Lisa K. Behrens[1], Andreas Hilboll[1,2], Andreas Richter[1], Enno Peters[1,*], Henk Eskes[3], and John P. Burrows[1]

[1]Institute of Environmental Physics (IUP-UB), University of Bremen, Bremen, Germany
[2]MARUM - Center for Marine Environmental Sciences, University of Bremen, Bremen, Germany
[3]Royal Netherlands Meteorological Institute (KNMI), De Bilt, the Netherlands
[*]now at: Deutsches Zentrum für Luft und Raumfahrt (DLR), Bremerhaven, Germany

Correspondence to: Lisa K. Behrens (lbehrens@iup.physik.uni-bremen.de)

Abstract. In this study, we present a novel NO_2 DOAS retrieval in the ultraviolet (UV) spectral range for observations from the Global Ozone Monitoring Instrument 2 on board EUMETSAT's MetOp-A (GOME-2A) satellite. We compare the results to those from an established NO_2 retrieval in the visible (vis) spectral range from the same instrument and investigate, how differences between the two are linked to the NO_2 vertical profile shape in the troposphere.

As expected, radiative transfer calculations for satellite geometries show that the sensitivity close to the ground is higher in the vis than in the UV spectral range. Consequently, NO_2 slant column densities (SCDs) in the vis are usually higher than in the UV, if the NO_2 is close to the surface. Therefore, these differences in NO_2 SCDs between the two spectral ranges contain information on the vertical distribution of NO_2 in the troposphere. We combine these results with radiative transfer calculations and simulated NO_2 fields from the TM5-MP chemistry transport model to evaluate the simulated NO_2 vertical distribution.

We investigate regions representative of both anthropogenic and biomass burning NO_2 pollution. Anthropogenic air pollution is mostly located in the boundary layer close to the surface, which is reflected by large differences between UV and vis SCDs of $\sim 60\,\%$. Biomass burning NO_2 in contrast is often uplifted into elevated layers above the boundary layer. This is best seen in tropical Africa south of the equator, where the biomass burning NO_2 is well observed in the UV, and the SCDs difference between the two spectral ranges is only $\sim 36\,\%$. In tropical Africa north of the equator, however, the biomass burning NO_2 is located closer to the ground, reducing its visibility in the UV.

While not enabling a full retrieval of the vertical NO_2 profile shape in the troposphere, our results can help to constrain the vertical profile of NO_2 in the lower troposphere and, when analysed together with simulated NO_2 fields, can help to better interpret the model output.

1 Introduction

Nitrogen dioxide (NO_2) is an important indicator for natural phenomena and anthropogenic air pollution, as it is produced in the troposphere by, e.g., biomass burning or combustion of fossil fuels (Lee et al., 1997). Additionally, NO_2 is produced by lightning (Lee et al., 1997; Beirle et al., 2004) and microbiological activity in soils (Williams et al., 1992; Bertram et al., 2005). The relevance of the individual NO_2 sources depends on the region of the Earth (van der A et al., 2008). Biomass burning is important in equatorial regions like central Africa, whereas anthropogenic emissions are mostly important in the industrialised mid-latitudes like China or Europe. The distribution of NO_2 is of major interest because it is harmful to human health, adds to local radiative forcing, catalyses surface ozone production during summer smog, and causes acid rain (Finlayson-Pitts and Pitts, 1999).

Using spectrometers, solar radiation scattered in the Earth's atmosphere can be measured and the amount of trace gases inverted mathematically from the depth of molecular absorption bands. Such measurements have been made from satellite (e.g., Burrows et al., 1999), airborne (e.g., Heue et al., 2005; Wang et al., 2005), and ground-based (Noxon, 1975) platforms.

Since hyperspectral satellite observations began in the mid-1990s (Burrows et al., 1999), the horizontal distribution of the column amounts of many trace gases is well known, e.g., for NO_2. Using sun-synchronous orbits, a nearly daily global coverage at similar local times can be obtained. The global coverage as well as the spatial resolution of the measurements depends on the instrument (see for example: Callies et al., 2000). However, there is only limited knowledge of the vertical distribution from satellite data. Compared to satellite observations, ground-based Multi AXis Differential Optical Absorption Spectroscopy (MAX-DOAS) measurements have high temporal resolution and can provide vertical profiles of trace gases up to several kilometres altitude (Wittrock et al., 2004), but can only measure at one particular location and are thus limited in resolving horizontal gradients.

Irrespective of the instrument's viewing geometry, the measured spectra can be analysed using the Differential Optical Absorption Spectroscopy (DOAS; Platt and Stutz, 2008; Burrows et al., 2011) technique which is a well established method based on Lambert Beer's law describing the spectral reduction of the initial intensity of light due to absorption. The main result is the integrated concentration of trace gases $\rho(s)$ along the effective light path s which is called the total slant column density (SCD; Platt and Stutz, 2008; Burrows et al., 2011):

$$SCD = \int \rho(s) ds. \tag{1}$$

As Rayleigh scattering in the atmosphere depends strongly on wavelength (λ; the scattering cross-section is proportional to λ^{-4}), sunlight having longer wavelengths can penetrate deeper into the atmosphere compared to shorter wavelengths. This results in a wavelength-dependency of the SCDs (Burrows et al., 2011). Consequently, if NO_2 is located close to the ground, SCDs retrieved from satellite measurements at shorter wavelengths are in theory smaller than SCDs retrieved from longer wavelengths. In consideration of this fact, knowledge of the vertical distribution of NO_2 can be gained by combining measurements at different wavelengths. The idea of using the penetration depth in the UV to determine trace gas vertical profiles was first proposed for ozone by Singer and

Wentworth (1957). The use of the temperature dependence of the Huggins absorption bands coupled with penetration depth was proposed to retrieve information about the vertical profile of ozone in the troposphere (Chance et al., 1997). Here, will use a similar method for the optically thin gas NO_2.

In the presence of clouds, the described behaviour changes. For cloudy scenes only smaller differences are expected. Due to the clouds the sensitivity towards the surface is decreased, and therefore, the NO_2 below the clouds is partly invisible to the instrument. For the NO_2 above the clouds, the sensitivity is similar or partly increased for the UV spectral range (Burrows et al., 2011). In previous studies, clouds at different altitudes have been used to obtain information about NO_2 profiles (Choi et al., 2014; Belmonte Rivas et al., 2015).

The vertical column densities (VCDs) are the integral of the trace gas concentration from the surface to the top of the atmosphere along the altitude z (Platt and Stutz, 2008; Burrows et al., 2011):

$$VCD = \int \rho(z) dz. \tag{2}$$

They can be calculated using air mass factors (AMFs), which are defined as the ratio of SCDs and VCDs (Platt and Stutz, 2008; Burrows et al., 2011), and are an indicator of the measurement sensitivity or the length of the light path within the NO_2 layer relative to the vertical path:

$$AMF(\lambda) = \frac{SCD(\lambda)}{VCD}. \tag{3}$$

AMFs are calculated by radiative transfer models, which take into account the viewing geometry and environmental effects (Platt and Stutz, 2008). The sensitivity of the measurement to an absorber varies with altitude; this is expressed by the so-called box air mass factor (BAMF; Burrows et al., 2011), which is defined as $BAMF_i = SCD_i/VCD_i$ for an atmospheric layer i. For wavelengths in the UV, the BAMF in layers close to the ground is considerably smaller than for the vis spectral range (Fig. 1). This reduction in sensitivity to lower atmospheric layers is further reduced for longer wavelengths. Figure 1 shows an example for surface type soil which results in a stronger altitude dependency compared to other surface types e.g., vegetation. In general, BAMFs for longer wavelengths have a smaller dependency on altitude compared with BAMFs for shorter wavelengths (Burrows et al., 2011).

Furthermore, the surface spectral reflectance (SSR) depends on the wavelength, and therefore, the wavelength dependence of the SCDs is influenced by the SSR (Burrows et al., 2011). Generally, for the UV and vis spectral range the SSR is quite low between 2 and 30 % depending on the surface type except for snow or ice (Burrows et al., 2011). For this kind of surface types, the SSR is lower in the UV than in the vis spectral range. For smaller SSR, the UV sensitivity shows a stronger decrease and for larger SSR (e.g. snow) a stronger increase towards the surface, resulting in corresponding SCD decreases or increases compared to the vis SCDs. Furthermore, the altitude of highest sensitivity depends on the SZA. For increasing SZAs, the altitude of highest sensitivity moves upwards to the stratosphere. Additionally, aerosols influence the measurements and also the visibility of NO_2 is influenced by the presence of aerosols (Burrows et al., 2011). Depending on the type and the optical thickness of aerosols the influences on the measurement differs.

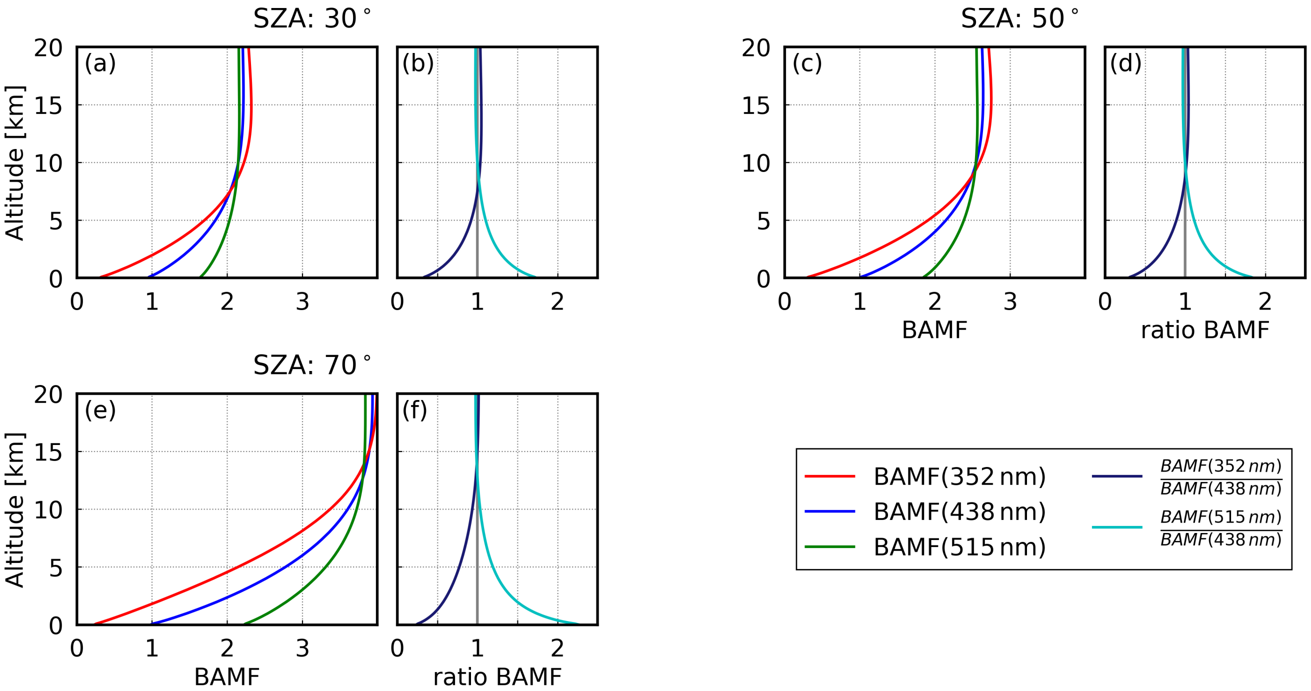

Figure 1. BAMF for UV (red line), green (green line), and blue (blue line) spectral range and the ratio of UV and green BAMFs calculated with the radiative transfer model SCIATRAN. BAMFs converge at higher altitude (not shown). The BAMFs are calculated for 352 nm (UV), for 438 nm (vis_blue), and for 515 nm (vis_green) at (a, b) 30° (c, d) 50° and at (e, f) 70° SZA. A surface spectral reflectance of 0.04 (352 nm), 0.06 (438 nm), and 0.09 (515 nm) representative for bare soil is assumed.

Another parameter needed for the AMF calculation is an a-priori NO_2 profile (Burrows et al., 2011), as the total AMF is calculated as the average of the BAMFs of all atmospheric layers, weighted by the absorber concentration. The retrieved VCDs therefore depend on the a-priori NO_2 profiles, and differences between the a-priori and actual NO_2 profiles can introduce systematic errors in the VCDs. As in principle, the final VCDs should not depend on the wavelength, analysing the differences in the VCDs retrieved from different wavelength regions allows to infer the validity of a-priori NO_2 profiles.

Typically, NO_2 DOAS fitting windows used in satellite data analysis are in the blue spectral range (see for example: Richter et al., 2011 and van Geffen et al., 2015). One satellite NO_2 retrieval using UV wavelengths has been developed for the Ozone Mapper and Profiler Suite (OMPS) on board of the Suomi National Polar-orbiting Partnership (SNPP) satellite, employing a DOAS-like method to derive NO_2 VCDs (Yang et al., 2014). Compared to VCDs retrieved in the blue spectrum with DOAS from the Ozone Monitoring Instrument (OMI) on board the Aura satellite, Yang et al. found good agreement between the two retrievals.

Richter and Burrows (2000) introduced also a NO_2 fitting window in the UV as well as in the green spectral range to retrieve tropospheric VCDs from GOME measurements. They conclude that it is possible to retrieve NO_2 from both spectral ranges and that stratosphere and troposphere can be separated by combining the two retrievals. However, the green spectral range is strongly influenced by liquid water absorption and interferences with vegetation and therefore, a reliable global retrieval of NO_2 was therefore not possible from the green spectrum.

In the present study, we introduce a DOAS retrieval for NO_2 in the UV spectral range and compare the results with a DOAS retrieval in the blue spectral range, which is our standard approach, to investigate the vertical sensitivity of satellite-based NO_2 measurements. Furthermore, we present a case study for the green spectral range for China. In Sect. 2, the NO_2 DOAS retrieval in the UV spectral range will be introduced for measurements from the Global Ozone Monitoring Experiment 2 (GOME-2) on board MetOp-A. The UV NO_2 retrieval settings will be discussed in detail and the dataset from the blue and green spectral range will be presented. In Sect. 3, results for the two/three NO_2 retrievals in the UV, green, and blue spectral ranges will be compared, and their implications for the NO_2 vertical distribution will be discussed. The manuscript ends with a summary and conclusions in Sect. 4.

2 Datasets and methods

2.1 The GOME-2A instrument

Different types of remote sensing instrumentation on satellite platforms yield spectral radiance at the top of the atmosphere, which contains information on the amounts and distribution of NO_2 in the Earth's atmosphere. Here, we use the GOME-2 instrument (Callies et al., 2000; Munro et al., 2016) on board the MetOp-A satellite (hereafter GOME-2A), which has a swath width of 1920 km, resulting in nearly global coverage every day. MetOp-A was launched in October 2006 into a sun-synchronous orbit with an equator crossing time of 09:30 local time (LT) in descending node. The GOME-2A instrument is a nadir viewing spectrometer with a ground pixel size of $80 \times 40\,\mathrm{km}^2$ (Callies et al., 2000). In July 2013, the ground pixel size was reduced to $40 \times 40\,\mathrm{km}^2$, when the identical GOME-2 instrument on board MetOp-B (hereafter GOME-2B), launched in September 2012, took over operational measurements (Munro et al., 2016). The spectrometer is separated into four channels covering wavelengths from 240 to 790 nm (Callies et al., 2000). Channel 2 provides data in the UV spectral range from 311 to 403 nm with a spectral resolution of 0.26 to 0.28 nm, while channel 3 provides data in the vis spectral range from 401 to 600 nm with a spectral resolution of 0.44 to 0.53 nm. These two channels are used for the following analysis.

2.2 NO_2 DOAS retrieval in the UV spectral range

For this study, we developed a NO_2 DOAS retrieval for the GOME-2A instrument in the UV which uses a fitting window between 342 and 361.5 nm, and a polynomial of degree four. In this retrieval, one NO_2 cross section measured with the GOME-2A instrument before launch, as well as two O_3 cross sections are used with an additional I_0

correction of 10^{20} molec cm^{-2} (Platt et al., 1997; Richter, 1997). Additionally, cross sections for O_4, BrO, HCHO, the Ring effect and the instrumental cross section Zeta are included in the fitting procedure (see Tab. 1).

Table 1. Fit settings for the NO_2 retrievals in the UV and the vis spectral range.

	UV spectral range	vis$_{\text{blue}}$ spectral range	vis$_{\text{green}}$ spectral range
fitting window	342 – 361.5 nm	425 – 450 nm	490 – 540 nm
polyn. degree	4	4	7
cross sections			
NO_2	223 K; Gür et al. (2005)	243 K; Gür et al. (2005)	243 K; Gür et al. (2005)
O_3	223 K and 243 K; Serdyuchenko et al. (2014)	223 K; Gür et al. (2005)	223 K; Serdyuchenko et al. (2014)
O_4	Greenblatt et al. (1990)	Greenblatt et al. (1990)	Greenblatt et al. (1990)
H_2O	–	Rothman et al. (2010)	Rothman et al. (2010)
BrO	Wilmouth et al. (1999)	–	–
HCHO	Meller and Moortgat (2000)	–	–
Ring	calculated with SCIATRAN, Vountas et al. (1998)		
instr. func.	Zeta; EUMETSAT (2011)	–	–

These settings are the result of a number of careful sensitivity tests. Among many different wavelength windows we tested, the selected window from 342 – 361.5 nm provided the smallest root mean squared error (RMS) of the fit residual. The instrumental correction function Eta (EUMETSAT, 2011) only had minor influence on the results when included in the fit; we therefore chose not to use it to keep the number of fit parameters small. Including additional O_3 cross sections to correct the O_3 non-linearity (Puķīte et al., 2010) improved the fit in polar latitudes, where solar angles and thus O_3 absorptions are large. However, this also introduced an offset in the data, and as we are mainly interested in polluted mid-latitudes, we chose not to use it here. Finally, we investigated the effect of using a daily Earth reflectance spectrum as reference instead of a daily solar reference. The differences between results using the two reference spectra were only minor so that we use the daily solar reference in order to preserve consistency with the fit in the blue wavelength region (see Sect. 2.3).

2.3 NO_2 DOAS retrieval in the visible spectral range

Due to the considerably stronger differential absorption lines in the blue compared to the UV spectral range (Fig. 2), NO_2 DOAS retrievals normally use measurements in the blue spectral range, see for example Richter et al. (2011) or van Geffen et al. (2015). Here for the blue spectral range, a retrieval from 425 − 450 nm with a polynomial degree of four is used (in the following vis_{blue}; introduced in Burrows et al., 1999 for the GOME instrument, applied to GOME-2A measurements in Richter et al., 2011). The fit settings are summarized in Tab. 1. Cross sections for NO_2 and O_3 are used for this retrieval. Additional cross section are O_4, H_2O, and the Ring effect.

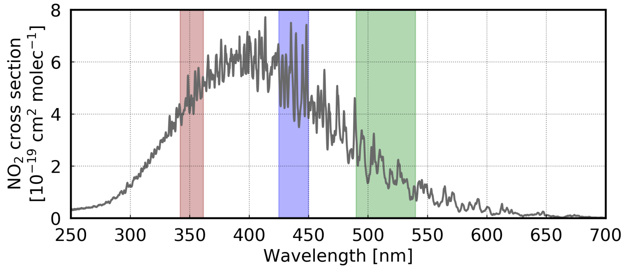

Figure 2. NO_2 absorption cross section measured at 243 K with the GOME-2 instrument now deployed on MetOp-A. The fitting windows used in this study are shaded by colour. Red: new NO_2 fitting window in the UV spectral range. Green: NO_2 fitting window in the green spectral range. Blue: NO_2 fitting window in the blue spectral range (see Tab. 1).

Furthermore, a second fitting window in the vis spectral range from 490 − 540 nm with a polynomial degree of seven is used (in the following $\text{vis}_{\text{green}}$; introduced in Richter and Burrows, 2000 for the GOME instrument). The cross sections used in this fit are NO_2, O_3, O_4, H_2O, and the Ring effect. The fit settings are shown in Tab. 1. The high polynomial degree of seven is chosen in order to correct for interferences with the surface and liquid water absorption. Including a liquid water cross section for the green spectral range introduces errors over land; therefore, no liquid water cross section is used in the NO_2 fit for the green spectral range.

2.4 Comparison of the NO_2 DOAS retrievals in the UV and visible spectral range

In the UV and green spectral range, the differential NO_2 absorption lines are weaker than in the blue spectral range. In Fig. 2 the NO_2 cross section (Gür et al., 2005) at 243 K measured with the GOME-2A instrument is shown. The wavelength dependency of the differential absorption strength is clearly observed. Furthermore, the measurement sensitivity for NO_2 decreases towards the surface. This can be clearly observed in the BAMF (Fig. 1). This effect is enhanced by the temperature dependency of the NO_2 cross section which is not taken into account in the DOAS fit. The temperature dependency influences the tropospheric as well as the stratospheric NO_2 measurements (see Fig. S4 and Fig. S5). For the stratospheric NO_2 the combined radiative transfer and temperature dependency leads to a 10% higher sensitivity in the UV spectral range than in the blue spectral range. Close to the surface, the temperature sensitivity is up to 10% stronger in the blue spectral range compared to the UV spectral range. For the green spectral range, the differences are less pronounced compared to the blue spectral range (Fig. S6 and Fig. S7). The green spectral range has a slightly reduced temperature sensitivity (up to 3 %) close to the ground and an enhanced sensitivity (up to 9 %) in the stratosphere compared to the blue spectral range. Additionally, the temperature vertical sensitivity introduces a seasonal and a latitudinal dependency. This effect is stronger in the tropics than for higher/lower latitudes and in the mid-latitudes it is more pronounced in summer and less in winter.

The smaller absorption lines in the UV in combination with reduced intensity from the sun and the weaker signal from the surface leads to a considerably higher noise level in the NO_2 differential optical depths in the UV spectral range compared to the blue. Similarly, in the green spectral range the absorption lines are smaller than in the blue spectral range and therefore, also the green spectral range has a higher noise level than the blue spectral range. To illustrate this, Fig. 3 shows an example of the fit results from different wavelength regions for one measurement above Teheran. As expected, the retrieved NO_2 SCD is smaller in the UV spectral range compared to the vis.

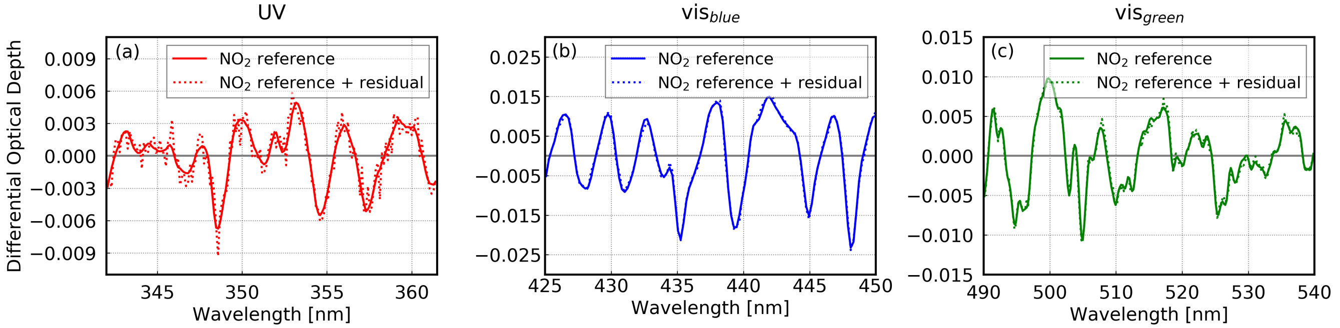

Figure 3. The NO_2 reference (differential NO_2 cross section multiplied with retrieved NO_2 SCD; solid line) and reference plus residual (dashed line) for the (a) UV, (b) blue, and (c) green spectral range for one pixel above Teheran (35.38° N, 51.47° E) on 22 January 2008. The SCD for this pixel for the UV spectral range is 6.31×10^{16} molec cm^{-2} with a fit error of 4.3 %, for the blue spectral range it is 9.33×10^{16} molec cm^{-2} with a fit error of 0.8 %, and for the green spectral range is 9.88×10^{16} molec cm^{-2} with a fit error of 0.9 %. Note the different y-axes.

Due to the noisier differential optical depth signal, the UV NO_2 fit has larger uncertainty compared to the vis$_{\mathrm{blue}}$ or the vis$_{\mathrm{green}}$ NO_2 fit. The UV NO_2 fit of the example has a random error of 4.3 %, whereas the vis$_{\mathrm{blue}}$ NO_2 fit has a smaller error of 0.8 %. The NO_2 fit in the green spectral range has only a slightly higher error than the blue fit with 0.9 %. Generally, the errors for the spectral ranges differ (see Tab. 2). For the estimation of the errors for the total SCDs over an assumed clean region (equatorial Pacific: 5° S to 5° N and from 150° E to 210° E) are calculated. In the blue spectral range, the standard deviation is smallest with 0.6×10^{15} molec cm^{-2} followed by the green spectral range with 1.4×10^{15} molec cm^{-2}. The highest scatter is found for the UV spectral range with 1.8×10^{15} molec cm^{-2}. This can also be seen in Fig. 4 which shows the distribution of total NO_2 VCDs over the selected region. Here, a stratospheric AMF was applied to calculate the NO_2 VCDs, as the common assumption is that no or very little tropospheric NO_2 is present in this area (Richter and Burrows, 2002; Martin et al., 2002; Peters et al., 2012). Due to the lower fit quality in the UV, the NO_2 columns retrieved there have a larger standard deviation of $7.4 \times 10^{14}\,\mathrm{molec\,cm^{-2}}$ compared to the $\mathrm{vis_{blue}}$ with a standard deviation of $2.1 \times 10^{14}\,\mathrm{molec\,cm^{-2}}$. For the green spectral range, a standard deviation of $5.8 \times 10^{14}\,\mathrm{molec\,cm^{-2}}$ is found. The green fitting window shows a bias to slightly more negative values over the Pacific Ocean which is related to liquid water absorption (not shown; see Sect. 2.3).

Table 2. Errors for the UV and vis spectral range.

	errors UV	errors $\mathrm{vis_{blue}}$	errors $\mathrm{vis_{green}}$
total SCDs	$1.8 \times 10^{15}\,\mathrm{molec\,cm^{-2}}$	$0.6 \times 10^{15}\,\mathrm{molec\,cm^{-2}}$	$1.4 \times 10^{15}\,\mathrm{molec\,cm^{-2}}$
	(STD calculated above the Pacific Ocean, see Fig. 4)		
total VCDs	$7.4 \times 10^{14}\,\mathrm{molec\,cm^{-2}}$	$2.1 \times 10^{14}\,\mathrm{molec\,cm^{-2}}$	$5.8 \times 10^{15}\,\mathrm{molec\,cm^{-2}}$
	(see Fig. 4)		
SSR	40% at 320 nm, Kleipool et al., 2008	5% at 500 nm, Kleipool et al., 2008	
0.05, increase 0.01	BAMF increases 9 % (338 nm, Lorente et al., 2017)	BAMF increases 11 % (440 nm, Lorente et al., 2017)	–
AMF			
cloud fraction	0 – 30%, Boersma et al., 2004		
cloud height	< 10%, Boersma et al., 2004		
aerosols	not included in our calculations → 15%, Boersma et al., 2004		
profile shape	< 15% (regions with little NO_2: > 50%), Boersma et al., 2004		

Furthermore, for VCD calculation several input parameters are needed (see also Sect. 2.7) which have further uncertainties. Several previous studies calculated errors for DOAS retrievals, as for example Boersma et al. (2004) and Lorente et al. (2017). Their results are summarized in Tab. 2. Additionally, the errors of the SSR differ strongly between the UV ($\sim 40\,\%$) and vis spectral range ($\sim 5\,\%$) which increases the uncertainty in the UV stronger (Kleipool et al., 2008). Overall, the uncertainties for the NO_2 concentration due to the SSR can be large, but in total it is smaller than 50 % (Boersma et al., 2004)

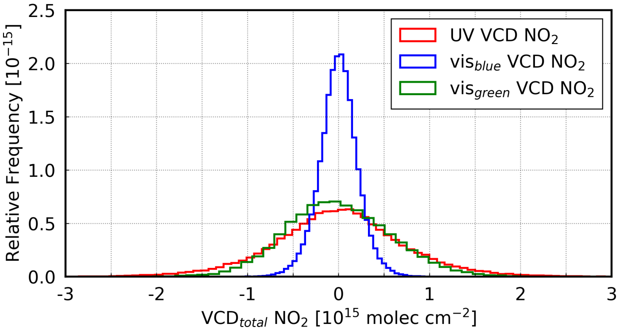

Figure 4. Distribution of total NO_2 VCDs over a clean region (equatorial Pacific: 5° S – 5° N and 150° E – 210° E) for three fitting windows in the UV, green, and blue spectral range for January 2008. Curves are normalized to unit area and centred on zero.

Generally, all three NO_2 retrievals lead to similar SCD spatial patterns. In Fig. 5, NO_2 SCDs for the UV, blue and green spectral range are shown for one orbit passing above East China on 03 January 2008. The larger uncertainty of the UV and $\text{vis}_{\text{green}}$ NO_2 retrieval is reflected in this figure by the larger spread of the slant columns and the existence of unphysical negative values. Nevertheless, the NO_2 columns in the UV spectral range and both vis spectral ranges are comparable for background regions and show a similar dependency on latitude. Over highly polluted regions, as for example China (25° N – 50° N), the vis NO_2 values are larger, especially the green spectral range, compared to the NO_2 values in the UV spectral range.

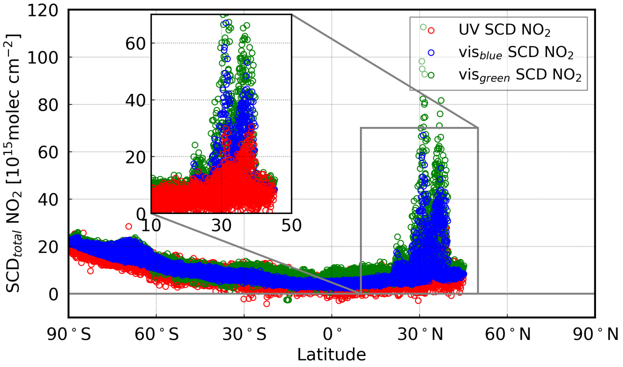

Figure 5. Total NO_2 SCDs of one orbit (above East China on 03 January 2008) for three fitting windows in the UV, blue, and green spectral range. Only data with SZA smaller 70° are shown.

2.5 Stratospheric NO_2

Stratospheric NO_2 shows large differences between the three spectral ranges. Figure 6 shows the latitudinal and seasonal dependency for the three NO_2 fitting windows. The seasonal dependency clearly differs between the three fitting windows also over regions dominated by stratospheric NO_2, especially for the green wavelength range, strong interferences are observable. Although the differences are smaller between the UV and blue spectral range, they are clearly observable, for example at the equator (Figure 6 b). In northern hemispheric summer the UV NO_2 values are higher than the NO_2 values derived from the blue spectral range whereas in northern hemispheric winter the NO_2 values from the blue spectral range are slightly higher. Consequently, the differences between the UV and blue spectral range have a clear seasonal dependency and therefore, it is currently not possible to consistently improve the stratospheric NO_2 retrieval by using different wavelength ranges as suggested in Richter and Burrows (2000).

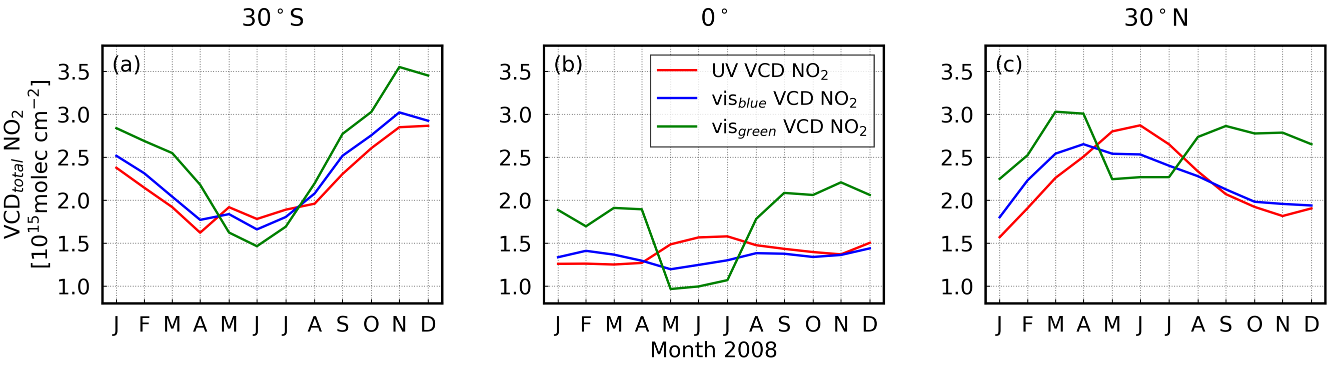

Figure 6. Time series of NO_2 total VCDs of 2008 for 30° S (averaged: 28° S – 32° S), 0° N (averaged: 2° S – 2° N), and 30° N (averaged: 28° N – 32° N) above the area of the reference sector for cloud free pixels.

2.6 Conversion to tropospheric NO_2 columns

For the comparison of tropospheric SCDs and VCDs, a correction for the impact of stratospheric NO_2 on the measured SCDs is needed. For the SCDs, we use the “reference sector method” (Richter and Burrows, 2002; Martin et al., 2002) for the three spectral ranges separately, in which a monthly average of SCDs measured over a presumably clean area above the Pacific (180° E to 210° E) is subtracted from all measurements per latitude band. The underlying assumption for this simple correction method is that no NO_2 is present over the reference sector in the troposphere, and that stratospheric NO_2 is zonally homogeneously distributed (Richter and Burrows, 2002; Martin et al., 2002). However, as this assumption is not always valid (Richter and Burrows, 2002; Boersma et al., 2004; Hilboll et al., 2013b), the reference sector method leads to areas with negative tropospheric NO_2 values, which are related to zonal inhomogeneities in stratospheric NO_2, for example close to the polar vortex (Dirksen et al., 2011). For the reference sector method, the same cloud screening as for the data selection is used (see Sect. 2.8). As the sensitivity to the stratosphere is similar in the three spectral ranges (see Sect. 2.7), the reference sector method is not expected to introduce systematic differences.

For the VCDs, we use a more sophisticated correction method, in which stratospheric VCDs from the Bremen-3D chemistry transfer model (B3dCTM, see Hilboll et al., 2013b and references therein) are used for the stratospheric correction. Therefore, no significantly negative values are expected for the VCDs assuming the model is correct. A Lambertian surface is assumed and the Lambert-equivalent reflectivity is taken as the SSR. For the AMF, a cloud correction is applied using the independent pixel approximation and cloud radiance fractions derived from the Fast REtrieval Scheme for Clouds from the Oxygen A-band (FRESCO+, version 6; Wang et al., 2008) dataset.

2.7 Radiative transfer simulations

The vertical sensitivity of the measurements to NO_2 has been investigated using BAMFs simulated for the UV (352 nm), the blue (438 nm), and the green (515 nm) fitting windows by the radiative transfer model SCIATRAN (version 3.6.5, see Rozanov et al., 2014). To calculate the radiance, SCIATRAN requires knowledge about the measurement scenario, e.g., viewing geometry, solar position, atmospheric absorbers, SSR, surface elevation, aerosols, and clouds as input parameters. Here, SSR and surface elevation have been taken from the OMLER_V003 (5-year climatology 2005 – 2009; wavelength: 354 nm, 442 nm, and 499 nm; Kleipool et al., 2008) and GMTED2010 (Danielson and Gesch, 2011) datasets, respectively. Exemplarily, results for 30°, 50° and 70° solar zenith angle (SZA) and SSR of 0.04 (352 nm), 0.06 (438 nm), and 0.09 (515 nm) are shown in Fig. 1. The SSR differs between the spectral ranges; the SSR values are chosen to be representative of soil which shows the strongest differences in BAMF close to the ground. For 50° SZA, the sensitivity at the surface in the blue is about three to four times larger than in the UV. The sensitivity in the green spectral range at this SZA is eight times higher than in the UV spectral range. In this wavelength range, the sensitivity at the surface depends stronger on SZA (for increasing SZA the differences between the two spectral ranges increase). The sensitivity difference between the wavelength regions decreases with increasing altitude, up to about 9 km, where they are identical. Above 9 km the UV shows a slightly (up to 4 %) higher sensitivity to NO_2 compared to the blue spectral range. The sensitivity of the green spectral range is slightly smaller (up to 3 %) than for the blue spectral range. With higher altitude the BAMFs converge, up to at around 30 km, from which onwards there are no significant differences between the spectral ranges (not shown). As shown in Fig. 1, the point of identical sensitivity moves upward with increasing SZA, which also influences the sensitivity in the atmosphere below the point of identical visibility. However, close to the ground, the differences between the UV and blue spectral range stay nearly constant.

In order to calculate the effective AMF for one measurement scene, the BAMF profile needs to be combined with an a-priori NO_2 concentration. This a-priori profile has a strong impact on the AMFs, as it provides the basis for the effective visibility of the NO_2 in the measurement scene. In this study, we used vertical NO_2 profiles from the TM5-MP model, described in Williams et al., 2017. For the European project QA4ECV (http://www.qa4ecv.eu) a 15 year run (2002 – 2016) was performed with the TM5-MP model version of July 2016. The model was run with a resolution of 1° × 1° on 34 levels, using ERA-Interim reanalysis meteorology from ECMWF, with a temporal sampling of 2 hours. This dataset has been used within the QA4ECV project as a-priori for the retrieval of e.g. formaldehyde, and for other projects such as the one described here. In particular, biomass burning emissions are taken from the monthly estimates provided by the GFEDv3 inventory (van der Werf et al., 2010), and latitude-dependent injection heights and a tropical burning cycle are implemented following Huijnen et al., 2010. See Williams et al., 2017 for other model details. In order to correct for the temperature dependency of the NO_2 cross-section, the NO_2 concentrations in each altitude are scaled by a correction factor linear in temperature for all spectral ranges, as suggested in Boersma et al., 2004. Temperatures were taken from the model; the temperature dependencies are illustrated in the supplement (Fig. S1 – Fig. S7).

2.8 Data selection and post-processing

The datasets for the three spectral ranges were gridded to a 0.25° × 0.25° grid and monthly means were calculated. Because of the fit quality and the reduced intensity in the UV spectral range, only measurements at solar zenith angles smaller than 70° are included in the following analyses. As a result of the fitting problems in the green spectral range (Sect. 2.3 and Sect. 2.4), in the following only time series for China are shown where the NO_2 concentrations are high and therefore, further influences are less pronounced (global maps are shown Fig. S11 – Fig. S14). Only measurements with a geometric cloud fraction smaller than 0.2 are included, unless otherwise noted. Cloud filtering was performed using the FRESCO+ (version 6) dataset (Wang et al., 2008). Furthermore, only fits with a χ^2 (describing the fit residual) smaller than 0.005 and 0.001 for the UV and vis spectral range, respectively, were used. While for the first years of the GOME-2A measurements, a consistent χ^2-limit could be used for all spectral ranges, instrumental degradation severely impacts the instrument's performance in later years (Dikty and Richter, 2011). Since channel 2 is more strongly affected by this degradation than channel 3, a larger χ^2-limit for the UV spectral range is needed for a statistically meaningful comparison.

3 Results and Discussion

3.1 Spatial distribution of NO_2 slant columns

Slant column densities (SCDs) are retrieved from the DOAS fit; they do not depend on any a-priori assumptions on the state of the atmosphere. Therefore, a comparison of the spatial distribution of the SCDs from the two UV and vis_{blue} fit windows provides a first opportunity to assess the NO_2. The SCDs depend on the VCDs and on the AMFs (see Eq. 3). Furthermore, the SCDs depend on the measurement geometry, SSR, and wavelength, and the AMFs additionally depend on the a-priori vertical NO_2 profile. Consequently, maps of SCDs show not only the altitude dependency, but also other changes of the AMF. For one particular measurement, the geometry is the same irrespective of the wavelength window. Thus, differences in the SCDs are introduced by the different sensitivities and therefore, large differences between the two spectral ranges are expected when the NO_2 is located close to the surface; when the NO_2 located higher in the atmosphere, the differences between the two spectral ranges are reduced. Consequently, the SCD differences can be partly explained by the different measurement geometries and SSR, which change during the year, but other factors like injection height and relative vertical distribution have to contribute as well.

Figure 7 shows monthly averages of tropospheric NO_2 SCDs for January and July 2008. In both spectral ranges, similar spatial patterns are found and anthropogenic as well as natural air pollution can be detected. Especially over the respective winter hemisphere, anthropogenic source regions are clearly observed. In January, for example, the highest NO_2 columns are located over China (a, b), whereas in July, there are high NO_2 values over the Highveld Plateau region in South Africa (HPSA; c, d). In addition, biomass burning regions are also clearly observable in the data. For instance, in July over Africa south of the equator (ASE), enhanced values are detected in both spectral ranges, consistent with van der A et al. (2008) and Schreier et al. (2014), who found a similar seasonal pattern. Finally, artefacts originating from the simplified stratospheric correction are observed in Fig. 7 (a, b), when enhanced NO_2 values over the Pacific reference area lead to large areas with too low NO_2 values in the subtropics of the northern hemisphere (see Sect. 2.6) in both spectral ranges.

In order to better compare the two NO_2 retrievals, Fig. 8 shows the relative differences between these results (absolute differences are shown in Fig. S15). Over highly polluted areas, NO_2 values in the UV spectral range are generally lower than in the blue spectral range (see Sect. 2.4). These differences are introduced by the wavelength dependency of the penetration depth (see Sect. 1), which leads to better visibility of lower tropospheric pollution to the vis_{blue} retrieval. Larger differences between the two NO_2 retrievals can be found in the respective winter hemisphere, e.g., in January over China and the east coast of the USA or in July over HPSA (see also Fig. 7). These large differences are related to both the larger tropospheric NO_2 SCDs and to the larger SZA (see Fig. 1). In addition, large differences are observed in the western South Atlantic, where the retrieval noise in both spectral ranges is strongly enhanced due to the South Atlantic Anomaly (Richter et al., 2011).

To further analyse the differences between the two spectral windows, we use the ratio of UV to vis_{blue} tropospheric NO_2 SCDs which is a first approximation of an altitude dependency; Fig. 9 shows these for (a) January and (b) July 2008. Highly polluted areas are clearly observable, with ratios as low as ~ 0.2, indicating the NO_2 being located close to the surface. As before, differences between the two retrievals are larger in the respective winter hemisphere, showing as lower ratios. The most obvious example is East China in January, where large areas with very low ratios can be detected. However, all strong anthropogenic source regions, e.g., India, northern America, HPSA, and the Middle East, but also individual large cities like Madrid, Moscow, and Mexico City, show low ratios between the two retrievals. Here, it should be noted that due to the rather strict selection criterion on the SZA (see Sect. 2.8), no data are available for the strong source regions in central Europe in January.

In addition to anthropogenic air pollution close to the ground, NO_2 pollution from biomass burning can be detected in the retrieval ratios, e.g., in ANE and ASE (Fig. 9). In July (southern hemispheric, SH, winter), values of ~ 0.6 are

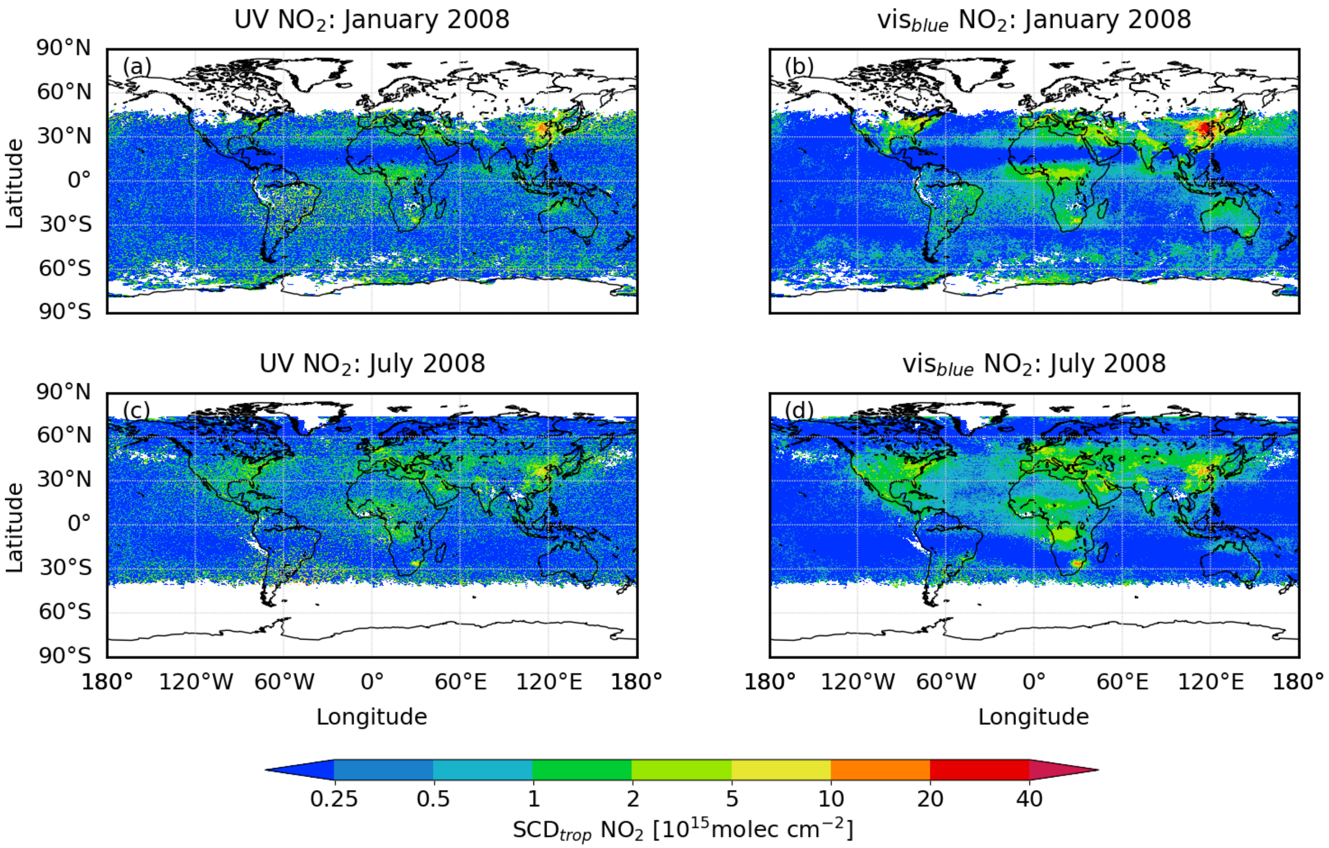

Figure 7. Monthly mean tropospheric NO_2 SCDs for (a, b) January and (c, d) July 2008. (a, c) UV spectral range and (b, d) blue spectral range.

found for the UV/vis$_{\text{blue}}$ ratio over the ASE region. These low values (as well as the absence of a signal in January) correspond to the seasonal pattern of biomass burning in this region.

In the ANE region, the vis$_{\text{blue}}$ fit results show clearly enhanced NO_2 SCDs in January (NH winter, coinciding with the annual biomass burning peak in this region) but not in July (see Fig. 7). However, no significant differences between the two months are observed in the UV fit results, where slightly enhanced values can be seen throughout the year (not shown). These findings will be further discussed in Sect. 3.2.

North of the ANE region at approx. $10° - 20°$ N, SCD ratios of ~ 0.7 can be found in July (see Fig. 9). This is an indicator for NO_2 enhancement most probably related to soil emissions (Jaeglé et al., 2004; Zörner et al., 2016). While this NO_2 is more clearly observed in the blue spectral region, also the UV results show enhanced SCDs (see Fig. 7). As shown by Delon et al. (2008) and Stewart et al. (2008), NO_x ($NO_x = NO + NO_2$) from soil emissions is usually well mixed and thus not only located close to the ground, but also in elevated layers, enhancing visibility in the UV.

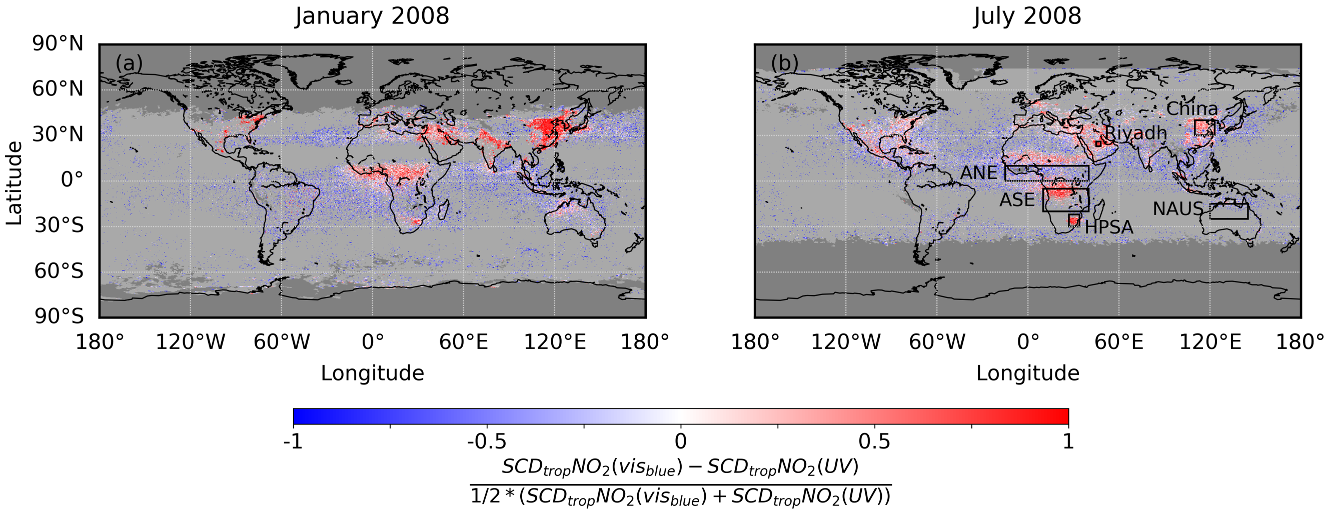

Figure 8. Relative difference between monthly mean tropospheric NO_2 SCDs in the UV and blue spectral range. Differences for (a) January and (b) July 2008. Dark grey shaded area: no NO_2 values available. Light grey coloured values indicate values where the vis_{blue} NO_2 is close to zero, which have been filtered out. This threshold was defined as a smoothed latitude-dependent mean over the reference sector area. The Pacific threshold is one standard deviation of the gridded NO_2 values for both retrievals. To smooth the latitude-dependent threshold, a 5°-running-mean was used. The regions defined in Tab. 3 are depicted in the right figure (b).

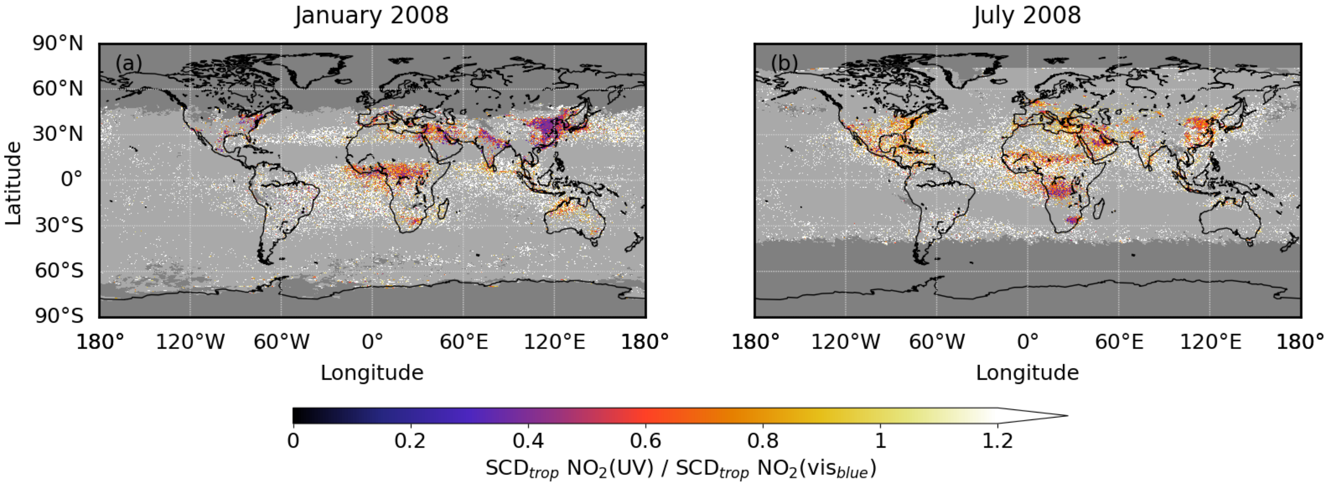

Figure 9. Ratio between monthly mean tropospheric SCDs of NO_2 in the UV and blue spectral range. (a) January 2008 and (b) July 2008. Dark grey shaded area: no NO_2 values available. Light grey coloured values indicate values where the vis_{blue} NO_2 is close to zero, which have been filtered out (Fig. 8).

Finally, Fig. 9 shows SCD ratios over the well known shipping lane leading from South India to the Strait of Malacca. The shipping signal in this region was first identified in satellite NO_2 data by Beirle et al. (2004) and Richter et al. (2004). Here, while the shipping lanes are clearly observable in the vis_{blue} SCDs, they cannot be identified in the UV NO_2 data. This is probably because the NO_2 shipping emissions stay with the shallow marine boundary layer. Consequently, the shipping emissions when averaged over the ground scene are below the detection limit for the UV spectral range (see Fig. 7). Higher horizontal resolution (e.g., in OMI and the upcoming S-5P, S-4, and S-5 missions) might improve detection of shipping lanes in the UV.

From the retrieved ratios of SCDs, a first approximation of the top-altitude of NO_2 can be calculated. For the altitude retrieval, simple box profiles from the surface up to a top altitude are assumed for tropospheric NO_2 and the ratios of these box profile SCDs are compared with the retrieve ratios of the measurements. The altitude of ratio from the box profile SCDs which fits best to the ratio of the measurement is taken as the NO_2 top-altitude. The retrieved top-altitudes for the individual pixels are shown in Fig. 10. A seasonal dependency of the retrieved altitude can be clearly observed in the global maps. Low altitudes are found in regions with low ratios e.g., China in January and HPSA in July. High altitudes are found over the Oceans and in the surroundings of highly polluted areas which is expected from transport events (Richter et al., 2014; Zien et al., 2014).

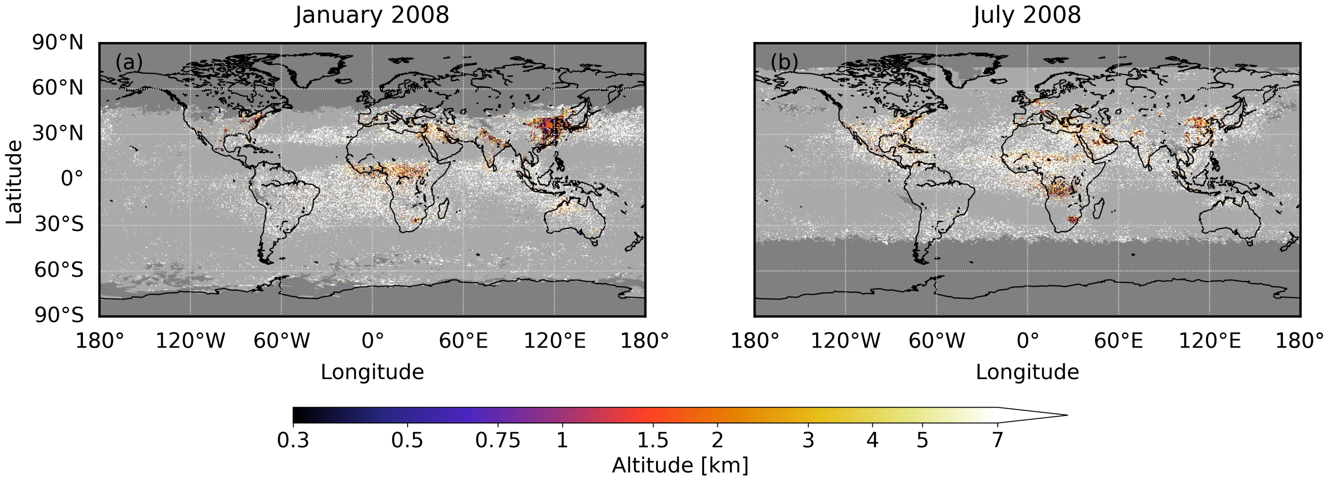

Figure 10. Monthly mean top-altitudes retrieved from the ratio between the UV and blue spectral range. To retrieve the altitude, box profiles are assumed for the tropospheric NO_2. Light grey coloured values indicate values where the vis_{blue} NO_2 is close to zero, which have been filtered out.

3.2 Temporal variability of regional NO_2 slant columns

In this section, we investigate the temporal variability of tropospheric SCDs from the two/three NO_2 retrievals over six regions (see Tab. 3 and Fig. 8 for the regions' definitions) and make inferences about the vertical distribution of NO_2 in the atmosphere. Figure 11 shows monthly mean time series for three natural / biomass burning source regions (a – c) and three anthropogenic source regions (d – f). The seasonal cycle observed in Fig. 11 a – c corresponds to the seasonal pattern of biomass burning activity in these regions (Schreier et al., 2014). Slightly negative SCDs in the UV fit in north Australia (NAUS; Fig. 11 c) and Riyadh (Kingdom of Saudi Arabia; Fig. 11 f) are artefacts caused by the stratospheric correction (see Sect. 2.6). Another artefact in the data is related to degradation of the GOME-2A instrument (see Sect. 2.8; Dikty and Richter, 2011), which is in some regions represented by a slightly decreasing linear trend (for example: in the UV in ANE and HPSA; Fig. 11 b and c).

Table 3. Selected regions for NO_2 time series with their abbreviation and their location.

Region	Abbreviation	geographical location
Africa south of the equator	ASE	5° S – 20° S and 10° E – 40° E
Africa north of the equator	ANE	0° N – 10° N and 15° W – 40° E
North Australia	NAUS	15° S – 25° S and 120° E – 145° E
China	—	30° N – 40° N and 110° E – 123° E
Highveld Plateau in South Africa	HPSA	22° S – 30° S and 27° E – 34° E
Riyadh	—	23° N – 26° N and 45° E – 48° E

In both ASE and NAUS, the seasonal cycles in the UV and blue spectral range are similar (Fig. 11 a and c), but the tropospheric NO_2 SCDs in the UV are smaller than in the blue spectral range. As can be seen in Fig. 12, this results in the strong correlation coefficients (0.87 in both cases, see Tab. 4) and slopes ≤ 1 of the regression lines (see Tab. 5). When the seasons are considered individually, the slope differs between 0.65 (biomass burning season) and 1.04 (rainy season). Hence, for both regions in the rainy season the two spectral ranges differ only by an offset whereas in the biomass burning season large differences are observed. Furthermore, in both regions for the individual seasons the correlation coefficient is also high (0.50 – 0.99; see Tab. 4), especially in the biomass burning season (≥ 0.92), which is probably related to the higher signal to noise ratio for this season. In ANE, conversely, significant differences in the seasonal cycle between the two spectral ranges can be observed, as the NO_2 signal from the biomass burning peak in NH winter shows in the blue spectral range only while in the UV, no interannual variability can be detected (Fig. 11 b). The increased NO_2 load observed in the vis_{blue} SCDs cannot be detected in the UV SCDs (nevertheless the correlation coefficient is 0.75). In all the other seasons, the correlation coefficient is comparable to that observed in ASE and NAUS (see Fig. 12 b and Tab. 4).

Several effects could contribute to an explanation for the differences in visibility of NO_2 in ANE in the two spectral ranges:

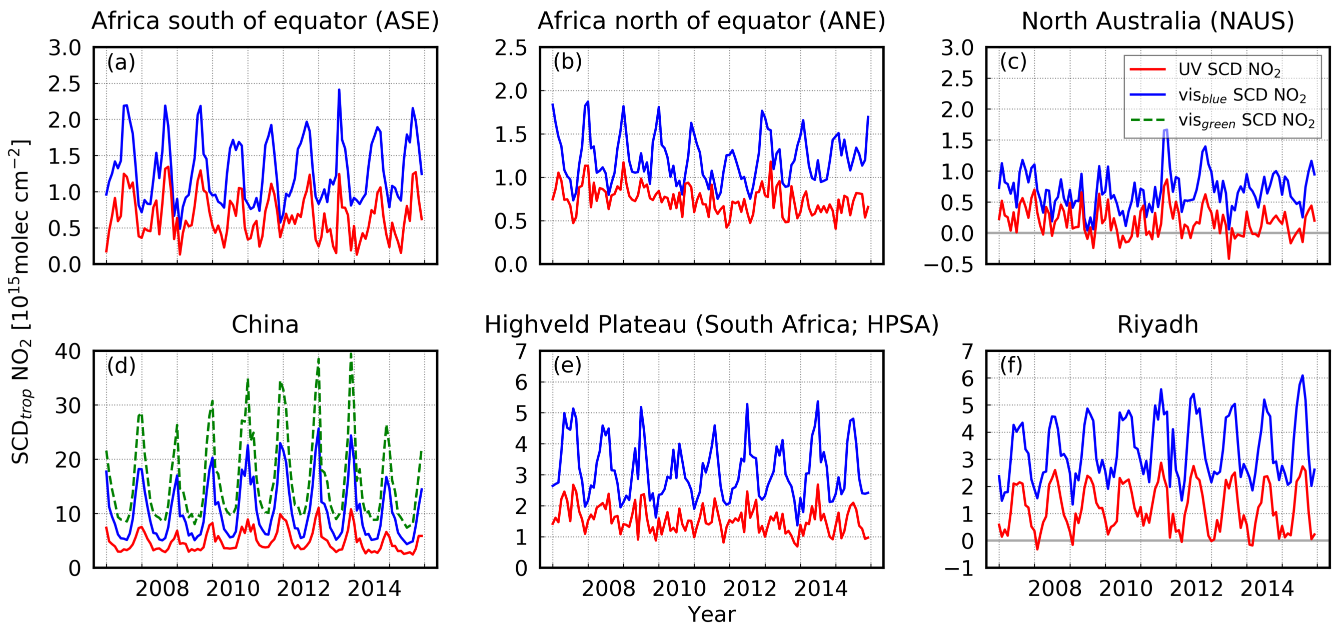

Figure 11. Time series 2007 – 2015 of tropospheric NO_2 SCDs for the UV (red line), $\mathrm{vis}_{\mathrm{blue}}$ (blue line), and $\mathrm{vis}_{\mathrm{green}}$ (green line, China only) spectral range for different regions. Note the different y-axes. The vertical lines indicate January of the individual years. (a – c) biomass burning regions and (d – f) regions with high anthropogenic air pollution.

Table 4. Correlation between UV NO_2 SCDs and $\mathrm{vis}_{\mathrm{blue}}$ NO_2 SCDs for the six selected regions.

Region	Annual	DJF	MAM	JJA	SON
ASE	0.87	0.50	0.69	0.92	0.80
ANE	0.53	0.75	0.77	0.76	0.63
NAUS	0.87	0.76	0.75	0.87	0.90
China	0.98	0.98	0.99	0.83	0.98
HPSA	0.82	0.74	0.80	0.90	0.87
Riyadh	0.95	0.73	0.86	0.70	0.95

1. Cloud influence on NO_2 measurements: When considering only those measurements flagged as cloudy (i.e., having a cloud coverage ≥ 0.3), only a weak seasonal cycle can be found in ANE (Fig. A1), whereas ASE shows a similar seasonal cycle in the cloud covered case as in the cloud free case. This indicates that the biomass

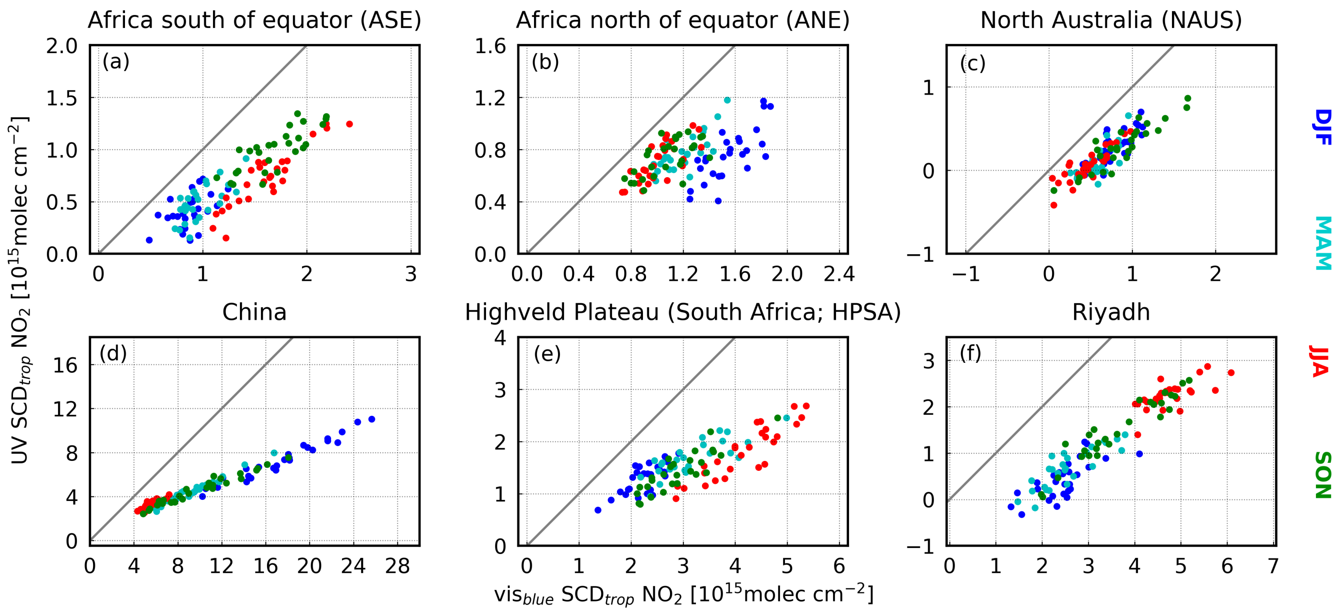

Figure 12. Scatter plot of tropospheric UV NO_2 SCDs against tropospheric vis$_{\text{blue}}$ NO_2 SCDs for the period 2007 − 2015 for the six selected regions. Note the different axes. The seasons are colour coded. The related correlation, slope and intercept of the regression line can be found in Tab. 4 and 5. December, January, February: DJF; March, April, May: MAM; June, July, August: JJA; September, October, November: SON.

burning NO_2 in ASE might be located partially in elevated NO_2 layers above the clouds, whereas in ANE NO_2 is located closer to the ground, i.e., usually below and thus partly shielded by the clouds.

2. NO_2 layer altitude: The altitude of biomass burning NO_2 emissions influence their visibility (see Fig. 1). According to simulations with the TM5-model (Williams et al., 2017; for details, see App. A2), the layer height of biomass burning NO_2 over ANE is lower than over ASE (Fig. A2). This is consistent with the above result, which shows high and low visibility for the biomass burning NO_2 in the UV for the ASE and ANE regions, respectively. For ASE, several previous studies could show that biomass burning plumes are regularly located at least partly above the boundary layer (Coheur et al., 2007; Rio et al., 2010; Gonzi and Palmer, 2010).

3. Stratospheric correction: For observations in the UV spectral range, total SCDs (i.e., the SCDs resulting from the DOAS fit, without the stratospheric correction described in Sect. 2.6) over ANE show two distinct peaks over the course of the year: one peak in NH winter and another peak in NH summer (Fig. A3). The NH winter peak in Dec./Jan. falls in the main biomass burning season and is thus expected to be of tropospheric origin. In contrast, the NH summer peak in May – July is of stratospheric origin, as stratospheric NO_2 has its maximum in summer. It is noteworthy that in the vis$_{\text{blue}}$ spectral range, this NH summer peak is smaller compared to

the UV, which might be partly related to small differences in the stratospheric sensitivity between the two wavelength ranges. In the UV SCDs, the biomass burning NO_2 might thus be obscured by the stratospheric correction due to the similar magnitude of the stratospheric NH summer peak.

4. Cloud influence on data sampling: The data shown in Fig. 11 are filtered to include only measurements not strongly influenced by clouds. In satellite-based cloud retrievals, smoke is often misinterpreted as cloud (Boersma et al., 2004). Assuming that smoke and NO_2 from biomass burning is advected together, this could lead to large parts of the biomass burning NO_2 being filtered out due to apparent cloud contamination of the measurement. However, the $\mathrm{vis}_{\mathrm{blue}}$ NO_2 SCDs are clearly enhanced in the cloud-free measurements, showing that not all biomass burning NO_2 is filtered out. Furthermore, there are only small differences in the cloud coverage between ANE and ASE (not shown); in both regions, the number of pixels being filtered out due to cloud contamination is similar. The minimum fraction of cloud free pixels is about 30 %, observed during the rainy season, while the maximum fraction of about 70 − 80 % and 80 % in ANE and ASE, respectively, is observed during the dry season, when the biomass burning occurs. It seems thus unlikely that the cloud filtering significantly impacts the visibility of the biomass burning NO_2 over ANE.

5. Aerosols: The NO_2 measurements could be influenced by aerosols. According to CALIPSO measurements, the main aerosol-type in ASE is smoke from biomass burning, while other aerosol types contribute only a smaller amount to the total aerosol concentration (Omar et al., 2009; Fig. A4). In contrast, the dominant aerosol-types in ANE are dust and polluted dust (Omar et al., 2009). As in the UV spectral range, the single scattering albedo (SSA) of dust is smaller than that of biomass burning aerosols (Russell et al., 2010; Dubovik et al., 2001; Bergstrom et al., 2007), the biomass burning NO_2 signal in ANE could be shielded by the darker dust aerosol in the UV. However, this hypothesis seems unlikely, as the number of dust aerosols (per area) is even higher in Riyadh compared to ANE, while in Riyadh a clear NO_2 seasonal cycle can be identified in both spectral ranges.

In summary, we conclude that the absence of a biomass burning NO_2 signal in the UV spectral range over ANE is predominantly formed by the lower injection height, causing the NO_2 to be located lower in the atmosphere compared to ASE. Due to the strong differences in sensitivity between UV and blue spectral ranges close to the ground, this could to a large extent explain the invisibility of UV NO_2 in ANE. However, also further effects could influence the visibility. For example, interferences of the seasonal cycles of stratospheric and tropospheric NO_2 over ANE might contribute, while we deem the effect caused by differing prevalent aerosol types in the three regions unlikely to be significant.

Figures 11 d − f show three regions dominated by anthropogenic air pollution. Here, absolute differences between UV and $\mathrm{vis}_{\mathrm{blue}}$ NO_2 values are often larger than in biomass burning source regions (see also Fig. 9). The seasonal cycle is mostly larger in the blue spectral range compared to the UV spectral range, indicating a seasonal dependency of the reasons underlying the differences between the spectral regions. In general, the time series of the two spectral ranges show a similar behaviour and are highly correlated (0.82; Tab. 4).

Over East China, the NO_2 SCDs in UV, $\text{vis}_{\text{green}}$, and vis_{blue} have similar shape and show a very high correlation of ≥ 0.98 (Fig. 11 d; see also Table S1). Until 2012, increasing NO_2 winter values in the three spectral ranges can be observed; these increases have been analysed in depth by Richter et al. (2005) and Hilboll et al. (2013a). In 2013, there are nearly no changes in NO_2 and afterwards, NO_2 SCDs are slightly decreasing, which was already reported by Richter et al. (2015) and Irie et al. (2016) and is consistent with findings reported by Hilboll et al. (2017) for anthropogenic NO_2 pollution in India. Over the HPSA region, no NO_2 trend is observed (Fig. 11 e). A clear seasonal cycle is observed in both spectral ranges, with the highest correlation coefficient in SH winter (0.90; Tab. 4). The detected seasonal cycle in the blue spectral range is similar to the cycle found by Noije et al. (2006) in the year 2000 in data from the Global Ozone Monitoring Experiment (GOME). In Riyadh (Fig. 11 f) a small trend is observed in maximum values. As shown by Hilboll et al. (2013a), during the whole period a slight increase can be detected. The detected month with maximum NO_2 is in agreement with van der A et al. (2008). In this area the NO_2 values derived from the UV and blue spectral range show a similar seasonal cycle and a similar year-to-year variability with a correlation coefficient of ≥ 0.95.

Table 5. Slope and intercept between UV NO_2 SCDs and vis_{blue} NO_2 SCDs for the six selected regions. Intercept in 1e15 molec cm^{-2}. In the brackets the standard errors for both values are shown.

Region	Annual	DJF	MAM	JJA	SON
ASE	0.66/ -0.19	0.98/ -0.45	0.96/ -0.44	0.83/ -0.61	0.65/ -0.10
	(0.03/ 0.05)	(0.23/ 0.20)	(0.17/ 0.16)	(0.07/ 0.11)	(0.09/ 0.15)
ANE	0.40/ 0.26	1.08/ -0.93	0.84/ -0.23	0.92/ -0.23	0.67/ 0.01
	(0.05/ 0.06)	(0.16/ 0.26)	(0.12/ 0.15)	(0.14/ 0.14)	(0.13/ 0.14)
NAUS	0.74/ -0.32	0.89/ -0.41	1.04/ -0.50	0.78/ -0.30	0.71/ -0.34
	(0.04/ 0.03)	(0.13/ 0.11)	(0.16/ 0 09)	(0.08/ 0.04)	(0.06/ 0.06)
China	0.37/ 1.04	0.42/ -0.07	0.46/ 0.25	0.49/ 0.52	0.37/ 0.89
	(0.01/ 0.08)	(0.02/ 0.30)	(0.02/ 0.14)	(0.06/ 0.36)	(0.02/ 0.16)
HPSA	0.41/ 0.24	0.74/ -0.37	0.46/ 0.21	0.68/ -1.03	0.60/ -0.32
	(0.03/ 0.09)	(0.12/ 0.26)	(0.06/ 0.21)	(0.06/ 0.27)	(0.06/ 0.19)
Riyadh	0.74/ -1.26	0.63/ -1.15	0.64/ -0.97	0.46/ 0.06	0.71/ -1.10
	(0.02/ 0.08)	(0.10/ 0.26)	(0.07/ 0.19)	(0.08/ 0.40)	(0.04/ 0.17)

In anthropogenically polluted areas, the differences in the NO_2 signal strength between the UV and blue spectral ranges are a result of the larger sensitivity to the lower troposphere in the blue spectral range. In winter the air pollution is mostly stronger, compared to summer, the SZA is higher, the boundary layer is more shallow (von Engel and Teixeira, 2013), and even within this boundary layer also a strong gradient is expected over high-emission areas (Dieudonné et al., 2013). All these effects increase the observed differences between the two spectral ranges. Due to the higher profile sensitivity close to the ground and the resulting larger differences, a lower regression slope (see Fig. 12) is observed for the anthropogenically polluted areas than for the biomass burning regions (Tab. 5) in all seasons. For example, in NAUS and ASE the regression line between all UV and vis_{blue} SCDs has a slope of 0.66 and 0.74, respectively, whereas for China and HPSA, a considerably smaller slope (~ 0.4) is found.

One has to note that the regions ANE and Riyadh do not follow this pattern — ANE due to the missing biomass burning NO_2 signal in the UV, and Riyadh probably because of differences in boundary layer height and the maximum in NO_2 seasonal cycle (von Engel and Teixeira, 2013). In Riyadh, the seasonal cycle of NO_2 emission and the cycle of the boundary layer height are in phase, as it is the case for naturally polluted areas, whereas for China and HPSA, the NO_2 maximum can be found in the respective winter season, where a lower boundary layer height is observed (Fig. S16). Consequently, in Riyadh the UV NO_2 signal is stronger and the slope (0.74) is larger than observed in other anthropogenic source regions.

Finally, a seasonal dependency of the regression line slope may result from the combination of the boundary layer height and concentration of NO_2. For ASE and NAUS, the slope shows a seasonal pattern, which might be influenced by the small signal to noise ratio (see Tab. 5). Slopes of ~ 1.0 can be found in these areas for the rainy season, with the largest uncertainties for these areas, possibly related to high cloud cover. The differences are thus most likely introduced by an offset. During biomass burning season, the slope is about 0.83 and 0.71 for ASE and NAUS, respectively. Since the biomass burning NO_2 signal cannot be seen in UV SCDs over ANE, no clear seasonal pattern can be observed there. In East China and the HPSA region, a larger slope can be found in summer, when the boundary layer is higher; spring, autumn and winter show a smaller slope (for China this can also be found for the green spectral range, Table S1). This is expected due to the increased sensitivity (see Fig. 1) of the UV measurements to NO_2 in a thick compared to a shallow boundary layer. In Riyadh however, this effect is not observed, possibly due to a decreased signal to noise ratio caused by the smaller area, entailing fewer measurements.

3.3 Spatial distribution of NO_2 vertical columns

The NO_2 vertical column densities (VCDs) are the final result of the DOAS retrieval procedure, as they are a physically meaningful and universally comparable quantity. In this section, we compare NO_2 tropospheric VCDs retrieved from the UV and the blue spectral range. For the calculation of the VCDs, NO_2 vertical profiles from the TM5-model (Williams et al., 2017) are used as a-priori (see Sect. 2.7). Assuming perfect measurements, radiative transfer simulations, and a-priori profiles, the AMF would equalise all differences between the two spectral ranges, leading to identical VCDs for UV and vis_{blue} fits. Figure 13 shows maps of monthly mean NO_2 VCDs for January and July 2008. The spatial patterns in both datasets are very similar and agree well with those shown in SCD maps (Fig. 7).

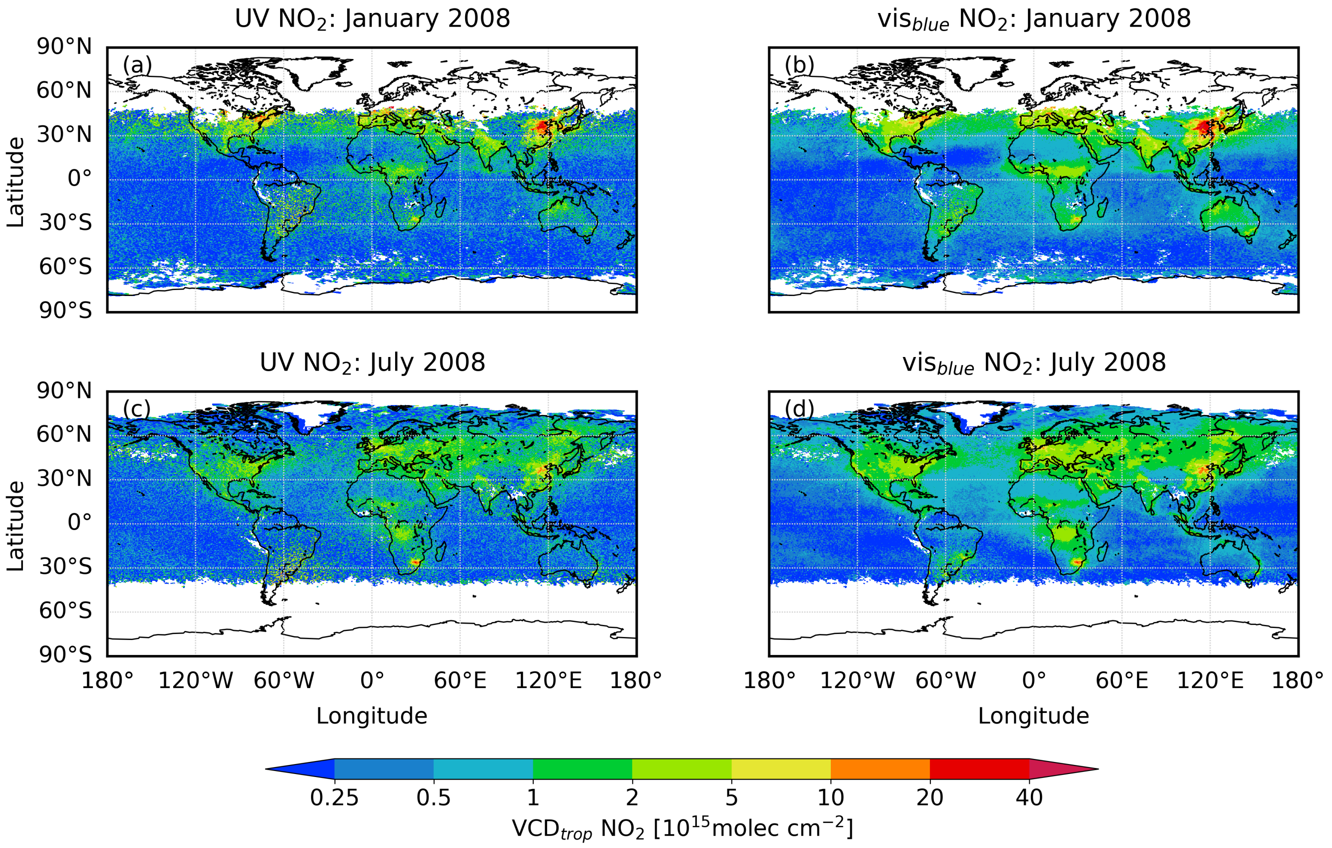

Figure 13. Monthly mean tropospheric NO_2 VCDs for (a, b) January and (c, d) July 2008. (a, c) UV spectral range and (b, d) blue spectral range.

However, also the VCDs of both spectral ranges do not perfectly match, as illustrated in Fig. 14. Compared to the relative differences of the SCDs shown in Fig. 8, the relative differences of the VCDs are smaller (absolute differences are shown in Fig. S17). Especially over areas without significant NO_2 sources, but also over the biomass burning regions, the differences between the two retrievals are reduced compared to the SCDs. Over anthropogenically polluted areas however, e.g., over China in January, the VCDs retrieved from the two spectral regions still show significant differences. The most probable reason for this is that the simulated NO_2 profiles used as a-priori do not represent the actual NO_2 vertical distribution; furthermore, aerosols and the SSR might influence the calculated VCDs, as will be discussed in Sect. 3.4.

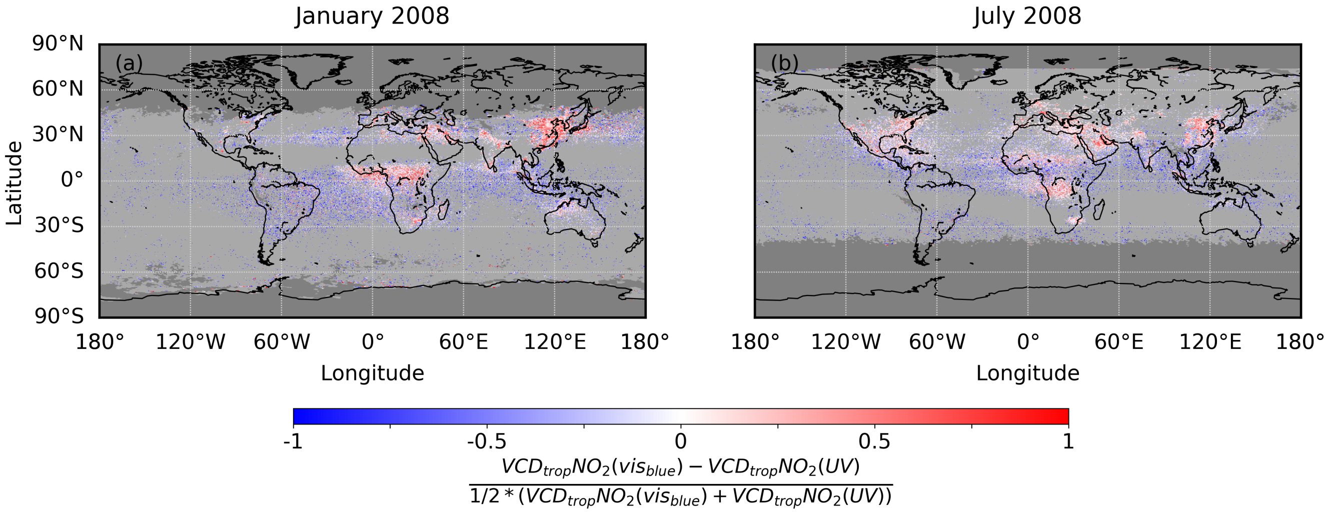

Figure 14. Relative difference between monthly mean tropospheric NO_2 VCDs in the UV and blue spectral range. Differences for (a) January and (b) July 2008. Dark grey shaded area: no NO_2 values available. Light grey coloured values indicate values which are filter out. The same filter as for Fig. 8 is used.

3.4 Temporal variability of regional NO_2 vertical columns

To better understand the reasons for the differences between the tropospheric VCDs of the two/three spectral regions, we again investigate the temporal variability over the six regions shown before (see Sect. 3.2, Tab. 3, Fig. 8 for the region definitions). The general shape of the seasonal cycles, which was described for SCDs in Sect. 3.2, can also be found in the VCD time series (Fig. 15). Similar to the SCD time series (see Sect. 3.2), the NO_2 VCDs are still mostly larger in the blue spectral range. Compared to the SCD differences, however, the VCD differences between the UV and the blue spectral range are reduced in all six regions (Fig. 15) which can also be seen in the larger slope of the regression line (Tab. 6). For nearly all regions and seasons, the slope of the regression line (Tab. 7) is still below one, indicating that the calculated AMFs are not representative for the actual state of the atmosphere. The SSR and the relative vertical profile as well as aerosols may contribute to the differences of VCDs between the UV and the blue spectral range.

In the ASE region, for example, the seasonal cycle in the VCDs is smoother than in the SCDs, especially for the UV data (Fig. 15 a). The seasonal cycles of the VCDs in the UV and the blue spectral range are more parallel, leading to a high correlation coefficient of 0.97 between the two data sets (see Tab. 6). However, rather than being separated by a simple offset, the VCDs from the two spectral ranges seem to be linearly related as indicated by the regression slopes differing from one (see Tab. 7 and Fig. 16). Compared to SCDs, the slope for the VCDs increases slightly in nearly every season; for the annual values, the slope of VCDs is 0.77 compared to 0.66 for SCDs.

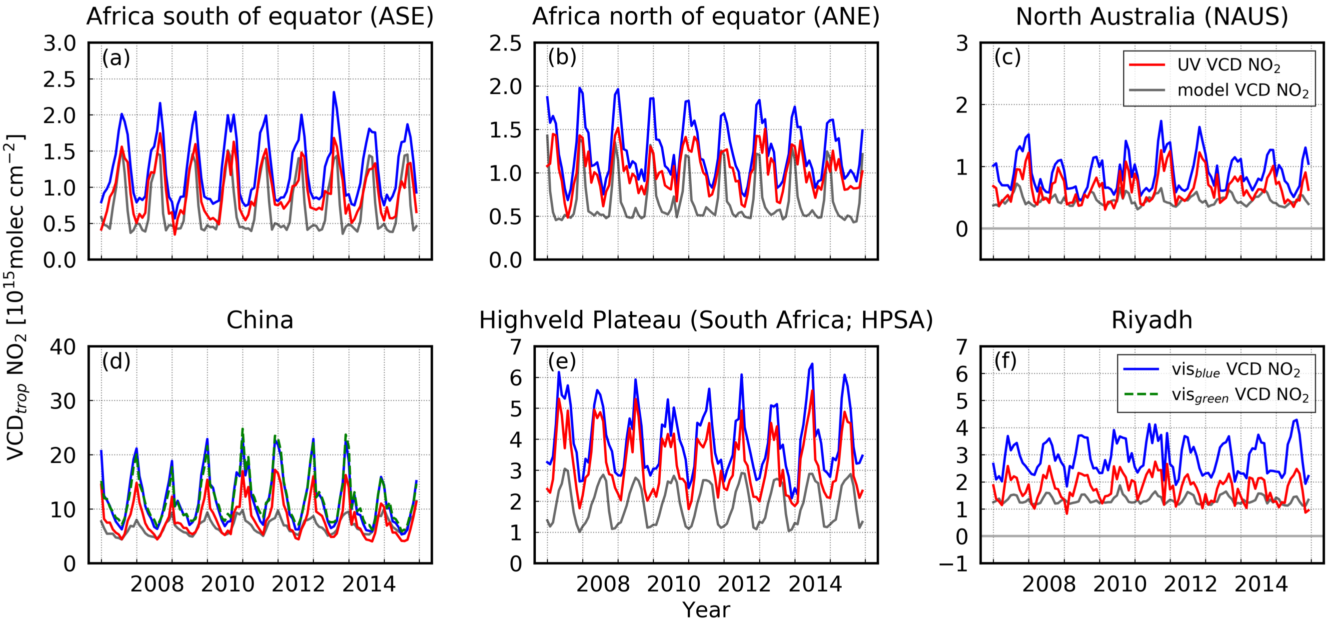

Figure 15. Time series 2007 – 2015 of tropospheric NO_2 VCDs for the UV (red line), vis$_{\mathrm{blue}}$ (blue line), and vis$_{\mathrm{green}}$ (green line, China only) spectral range as well as the TM5-model VCDs (grey line) for different regions. Note the different y-axes, the same as in Fig. 11. The vertical lines indicate January of the individual years. (a – c) biomass burning regions and (d – f) regions with anthropogenic air pollution.

Table 6. Correlation between UV NO_2 VCDs and vis$_{\mathrm{blue}}$ NO_2 VCDs for the six selected regions.

Region	Annual	DJF	MAM	JJA	SON
ASE	0.97	0.66	0.89	0.93	0.95
ANE	0.91	0.75	0.92	0.98	0.87
NAUS	0.95	0.92	0.78	0.93	0.94
China	0.98	0.96	0.98	0.96	0.97
HPSA	0.96	0.79	0.97	0.90	0.93
Riyadh	0.92	0.83	0.89	0.70	0.96

In the ANE region, the VCDs from the UV and blue spectral range agree considerably better than for the respective SCDs (Fig. 15 b). The UV NO_2 VCDs show a clear seasonal cycle, of similar shape but reduced amplitude compared to the vis$_{\mathrm{blue}}$ VCDs, leading to reduced differences between the two spectral ranges. Comparing to the SCDs in the ANE region, this indicates that the biomass burning NO_2 seems to be located too close to the ground to be detected by the UV retrieval; however, as the NO_2 emitted by fires is included in the simulation from which the a-priori profiles are taken, the AMFs introduce the observed seasonal cycle in the UV VCDs. This is reflected by the considerably improved correlation coefficients of 0.91 for all VCDs (see Tab. 6) compared to 0.53 for all SCDs; similar improvements can be seen for all seasons individually. Interestingly, when the seasons are considered separately, the regression line has higher slopes between 0.79 (SON) and 1.06 (JJA), showing that in the rainy season, the UV and vis_{blue} VCDs only differ by an offset. Nevertheless, discrepancies between the two spectral ranges are still observed, especially during biomass burning season.

For NAUS, the correlation coefficient between UV and vis_{blue} VCDs is higher (0.95) than for the SCDs (0.78). Also in this area, the slope of the VCD regression lines is constant or increased compared to the SCDs (Tab. 7; Fig. 16). During rainy season, the observed differences between UV and vis_{blue} VCDs are mostly related to an offset, whereas during biomass burning season the slope is smaller than one.

For VCD time series over East China (Fig. 15 d), the upward trend which was observed in the winter NO_2 SCDs (see Fig. 11 d) is not present in the VCDs. However, also here the UV NO_2 values are still smaller than the vis_{blue} NO_2 values. In spite of these discrepancies, the correlation coefficient is highest for this region (≥ 0.96 in all seasons). During all seasons the correlation coefficients are increased or similar compared to those of the SCDs. While the slope of the regression line is still smaller than one (0.59 – 0.76; Tab. 7), it is still increased compared to SCDs. The green and blue spectral range show a good agreement with a correlation coefficient of 0.98 (see also Table S2). Furthermore, the slope (1.07) agrees well which shows that there are only smaller differences between these spectral ranges.

The Highveld (HSPA, Fig. 15 e) region differs from all other regions: a high correlation coefficient (0.90) can be found in SH winter, when also the slope of the regression line (1.00) as well as the offset is high. In SH summer, however, the smallest correlation coefficient is observed for the region (0.79) and also the slope is the smallest with 0.77.

In Riyadh, large relative differences between the UV and blue spectral ranges can be found compared to the other regions (Fig. 15 f). This is reflected by the slope of the regression line which is ~ 0.75, except for NH winter when the slope is 1.19 with a large offset (Fig. 16 f).

The observed discrepancies between the UV and blue spectral ranges can result from different reasons: they can be related to the a-priori profiles used for VCD calculations, or they can be related to other influencing factors like aerosols and surface properties. The importance of the a-priori profile shape for the resulting VCDs was shown by Martin et al. (2002) and Boersma et al. (2004); the resulting uncertainty for this parameter is assumed to be smaller than 15 % (Boersma et al., 2004). A potential error in the a-priori profiles from the TM5-model in a given altitude layer will lead to different errors in the VCDs calculated for the UV and the blue spectral range, due to the spectral dependence of the measurement sensitivity (i.e., the a-priori error is weighted with different sensitivities in the two spectral ranges; see Fig. S18). Higher NO_2 concentrations close to the surface combined with a lower

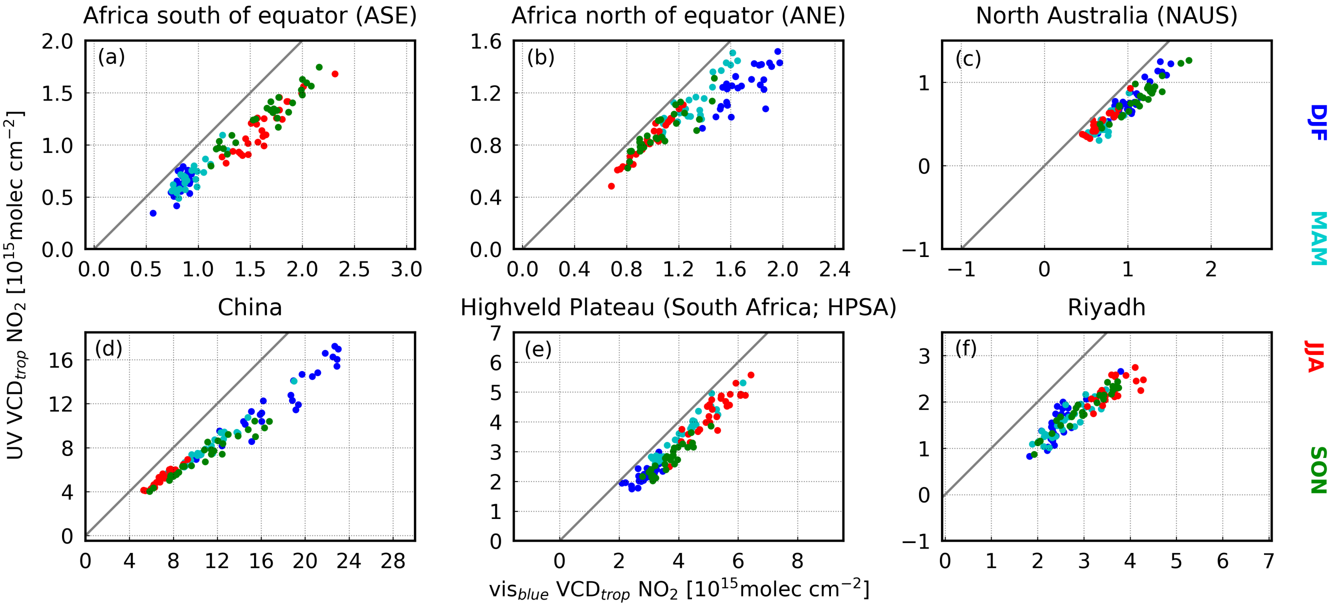

Figure 16. Scatter plot of tropospheric UV NO_2 VCDs against tropospheric vis$_{\text{blue}}$ NO_2 VCDs for the period 2007–2015 for the six selected regions. Note the different axes. The seasons are colour coded. The related correlation, slope and intercept of the regression line can be found in Tab. 6 and 7. December, January, February: DJF; March, April, May: MAM; June, July, August: JJA; September, October, November: SON.

injection height would reduce the differences between the UV and blue spectral range. The a-priori profile is especially relevant in biomass burning season, when the quality of the a-priori profiles is probably lower than usual, since the modelling of biomass burning emissions entails large uncertainties due to spatial resolution, emission uncertainties, and assumptions made on the plume injection height (see, e.g., Archer-Nicholls et al., 2015 and references therein). Similarly, since our retrieval does not explicitly account for the effect of aerosols, an aerosol layer at a given altitude will influence the visibility of the NO_2 both above and below the aerosol differently, enhancing the difference in the VCDs retrieved from the two spectral ranges. The same is true for potential errors in the assumed SSR. In order to bring UV and vis retrievals into better agreement, either the UV SSR would have to be lower than assumed or the vis SSR larger than assumed or a combination of both. As shown by Boersma et al. (2004), in March the uncertainties of NO_2 concentration are largest in polluted areas with low SSR, but they are generally below 50 % (see also Tab. 2).

Tropospheric model VCDs are plotted in Fig. 15, showing a regional dependency of the discrepancies between the model VCDs and the observed VCDs. For ASE and ANE during biomass burning season, the UV NO_2 VCDs and the model VCDs agree quite well, while the vis$_{\text{blue}}$ NO_2 values are higher. It should however be kept in mind that in the vis$_{\text{blue}}$ retrieval, both the uncertainties and the contribution of the a priori are lower, making these results more

Table 7. Slope and intercept between UV NO_2 VCDs and vis_{blue} NO_2 VCDs for the six selected regions. Intercept in 1e15 molec cm^{-2}. In the brackets the standard errors for both values are shown.

Region	Annual	DJF	MAM	JJA	SON
ASE	0.77/ 0.04	1.62/ -0.73	0.91/ -0.15	0.94/ -0.37	0.76/ 0.01
	(0.02/ 0.03)	(0.30/ 0.25)	(0.09/ 0.08)	(0.07/ 0.12)	(0.05/ 0.08)
ANE	0.69/ 0.15	0.90/ -0.29	1.04/ -0.24	1.06/ -0.21	0.79/ 0.06
	(0.03/ 0.04)	(0.14/ 0.23)	(0.08/ 0.11)	(0.04/ 0.04)	(0.08/ 0.09)
NAUS	0.81/ -0.07	0.98/ -0.24	1.12/ -0.30	0.94/ -0.12	0.78/ -0.08
	(0.03/ 0.02)	(0.08/ 0.09)	(0.16/ 0.11)	(0.07/ 0.05)	(0.06/ 0.07)
China	0.69/ -0.15	0.75/ -0.85	0.72/ -0.11	0.76/ -0.12	0.59/ 0.79
	(0.01/ 0.16)	(0.04/ 0.78)	(0.03/ 0.32)	(0.04/ 0.29)	(0.03/ 0.34)
HPSA	0.94/ -0.54	0.77/ 0.02	0.93/ -0.29	1.00/ -0.89	0.87/ -0.49
	(0.03/ 0.11)	(0.11/ 0.31)	(0.05/ 0.19)	(0.09/ 0.48)	(0.07/ 0.26)
Riyadh	0.74/ -0.37	1.19/ -1.43	0.79/ -0.51	0.67/ -0.19	0.74/ -0.37
	(0.03/ 0.09)	(0.15/ 0.36)	(0.08/ 0.20)	(0.12/ 0.42)	(0.04/ 0.12)

reliable. In rainy season, especially in ANE, there are larger discrepancies between the UV and vis_{blue} NO_2 and the model VCDs. The model values are lower though the UV and blue spectral ranges agree quite well. This confirms the above finding that the differences between the spectral ranges are caused by an offset. The differences during biomass burning season might be related to the aerosol treatment or wrong SSR in AMF calculations.

Also for NAUS the simulated and observed values agree quite well in the rainy season, whereas in the biomass burning season large differences between the three values are observed. Therefore, in this regions a combination of the different factors, described above, will most likely provide the best explanation.

For China and Riyadh, in the less polluted season the model and UV NO_2 values agree quite well whereas the vis_{blue} NO_2 values are larger. In the season with high air pollution, in both regions large discrepancies between the three values are observed. For anthropogenically polluted areas, the discrepancies between the modelled and the measured NO_2 values are well known from previous studies (e.g., Huijnen et al., 2010). For these regions, also aerosols play an important role and can further influence the differences between the two spectral ranges. As shown by Russell et al. (2010), especially dust reduces the visibility in the UV spectral range which could partly explain the differences in Riyadh. Additionally, as shown by Boersma et al. (2004), for these anthropogenically polluted areas also the SSR can introduce large differences. In China only small differences between the blue and green spectral range were found. The reason for the different behaviour between the two vis spectral ranges might be that the green spectral range is less sensitive to the a-priori profile compared to the UV and blue spectral range (see Fig. S18).

In HPSA, an offset between the model and the observed values can clearly be observed, which could partly explain the differences in SH winter values (Tab. 7). However, also here the SSRs and aerosols might influence the measurements, and therefore, the calculation of AMF.

4 Summary and Conclusion

In this study, we present a new NO_2 DOAS retrieval for measurements by the GOME-2A instrument, using the ultraviolet (UV) spectral range. Having NO_2 measurements from this wavelength range in addition to the usually exploited blue spectral region gives insights into the vertical distribution of tropospheric NO_2, as the vertical sensitivity of space-borne NO_2 DOAS retrievals strongly depends on the wavelength.

NO_2 slant column densities (SCDs) can in principle be retrieved from the UV spectral range, as shown by Yang et al. (2014). However, the UV retrievals have larger uncertainty compared to the blue spectral range, caused by the smaller differential absorption and the reduced intensity in the UV spectral range, leading to inferior fit quality, and also due to the larger AMF uncertainties. Nonetheless, the spatial distribution of both retrievals agrees very well.

We focused our analysis on six regions: three biomass burning regions (Africa south of the equator / ASE, Africa north of the equator / ANE, and northern Australia / NAUS), and three anthropogenic source regions (Eastern China, the Highveld Plateau in South Africa / HPSA, and the surroundings of Riyadh).

The differences between the UV and vis_{blue} fits are lower over the biomass burning areas ASE, ANE, and NAUS compared to the regions dominated by anthropogenic pollution. The NO_2 from biomass burning is in some regions and periods located in elevated layers, leading to an effectively smaller sensitivity difference between UV and blue spectral ranges. This is reflected by the slope of the regression lines between UV and vis_{blue} SCDs, which is 0.66 and 0.74 for the ASE and NAUS regions, respectively. Anthropogenic air pollution on the other hand is mostly located in the boundary layer close to the ground (see Stull, 1988). As the sensitivity of the UV retrieval drops sharply towards the surface, this leads to considerably lower regression line slopes of 0.37 and 0.41 for East China and HPSA, respectively. Nonetheless, SCDs in the UV and vis_{blue} show high correlation coefficients ≥ 0.82 in both cases.

In ANE, the biomass burning NO_2 in NH winter cannot be observed in the UV SCDs. Our analysis of UV NO_2 SCDs over cloudy scenes and of NO_2 profiles simulated by the TM5-MP model both suggest that in ANE the NO_2 is located close to the ground, where sensitivity in the UV is limited. The non-detectability could be increased by the stratospheric NO_2 seasonal cycle, which counteracts the biomass burning NO_2 signal over ANE. Moreover, the ANE biomass burning NO_2 could be shielded by the predominantly dust aerosols, which are dark in the UV and thus lead to decreased sensitivity compared to other biomass burning regions. In ASE, for example, the predominant aerosol type is smoke, which is brighter than dust in the UV spectral range; combined with the higher altitude of the NO_2 this leads to increased visibility in ASE.

In Riyadh, the seasonal cycles of boundary layer height and tropospheric NO_2 are in phase, contrary to other anthropogenically polluted areas, where NO_2 columns are highest in winter, when the boundary layer is shallow. Therefore, the maximum NO_2 values coincide with high boundary layers and thus better visibility in the UV fit, leading to better agreement between SCDs from the two spectral regions, expressed by a higher slope of the regression line of 0.74.

Even though in theory, given perfect measurements, radiative transfer modelling, and a-priori information, vertical column densities (VCDs) retrieved by the DOAS technique should be independent on the wavelength, VCDs retrieved from the UV and vis fits do still show considerable differences. If the a-priori profile does not capture the actual vertical distribution of NO_2 in the troposphere, the vertical measurement sensitivity will be incorrectly aggregated in the air mass factor calculation, which will lead to wavelength-dependent VCDs. Having said this, the observed VCD differences can also be introduced by further input parameters like surface spectral reflectance (SSR; wavelength: 354 nm and 442 nm) and the lack of explicit aerosol treatment. These parameters can lead to large discrepancies between the two spectral ranges when assumed wrongly. Even though differences exist between the UV and blue spectral ranges, the correlation coefficient between the VCDs is high everywhere (≥ 0.91). Generally, the differences between the two spectral ranges indicate that the NO_2 in the atmosphere is located in lower atmospheric layers than in the model which has stronger inferences in the UV, or the assumed SSR is too high in the blue spectral range.

While vis_blue NO_2 VCDs are often larger than UV VCDs, the latter agree with the simulated VCDs in most seasons. For China and HPSA, the differences between the UV and blue spectral ranges are pronounced in the respective winter season, whereas for Riyadh large differences can be found throughout the whole year. However in HPSA, in SH winter the correlation coefficient and the slope of the regression line is largest with an high offset. In the biomass burning regions, the agreement is better for the rainy seasons; during dry season, when a larger aerosol load is expected, the differences are larger. After conversion into VCDs, in ANE a clear seasonal cycle can be observed in both spectral ranges, which is mostly introduced by the a-priori assumptions in the AMF calculation.

An additional fitting window in the green spectral range also shows a higher uncertainty compared to the blue spectral range which is related to the smaller absorption lines as well as interferences with liquid water and vegetation, as already reported by Richter and Burrows (2000). Nevertheless, over highly anthropogenically polluted areas, NO_2 retrieved from the green spectral range is even more sensitive to the lower troposphere compared to the blue spectral range. This can be clearly observed in the higher vis_green SCDs over China compared with the UV and blue spectral range. In general, the SCDs of the three spectral ranges agree well with correlation coefficients ≥ 0.98. The VCDs for the green and blue spectral show also a good agreement (correlation coefficient of 0.98 and slope of 1.07) which might be related to the smaller sensitivity to the a-priori profile.

It is currently not possible to retrieve vertical profiles of tropospheric NO_2 from satellite measurements, due to the low information content of the measured spectra (see, e.g., Hilboll et al., 2014). Further developments in space-based observation of the Earth's atmosphere could however increase the capability to retrieve vertical NO_2 distribution. For example, concurrent measurements of the same air mass from different viewing geometries could yield insight on aerosol types and vertical profiles which might be also possible for GOME-2A and GOME-2B observations. This in turn would increase the possibility to retrieve more quantitative information about the vertical distribution of NO_2 in the troposphere. Improvements in signal to noise ratio would reduce the uncertainty in the UV retrievals and thus increase the value of the UV slant columns.

However, our study shows that even for the current generation of instrumentation in the global observing system, the difference between vis_{blue} and UV NO_2 DOAS retrievals can be used to constrain our knowledge of NO_2 vertical distribution in the lower troposphere. For example when coupled with data assimilation techniques and high resolution models the amount of boundary layer NO_2 and its trends can be inferred more accurately.

Appendix A: Shielding of northern hemispheric winter values in Africa north of the equator

A1 Shielding by clouds

Figure A1 shows NO_2 time series for cloud free scenes ($\leq 20\,\%$ cloud fraction; a and c) and for cloudy scenes ($\geq 30\,\%$ cloud fraction; c and d). The decrease/increase of NO_2 values in recent years shown in Fig. A1 is probably related to instrumental degradation (Dikty and Richter, 2011); a similar decrease/increase cannot be observed in GOME-2B data (not shown). In ASE, the seasonal cycles for cloud covered and cloud free measurements are similar. In ANE, however, only a weak seasonal cycle can be found for the cloudy scenes in either spectral range, whereas in the cloud free scenes a clear seasonal cycle can be found in the blue but not in the UV spectral range. This implies that the NO_2 layer over ASE could be located also in higher altitudes, while over ANE the NO_2 could be located closer to the ground and thus less sensitive to the UV observations.

A2 NO_2 profile shape

To compare the vertical distribution of NO_2 over the biomass burning areas ANE, ASE, and NAUS, simulated NO_2 concentration fields from the TM5-MP (Williams et al., 2017) for 2008 at 09:00 LT were used. We assume that the small time difference between the satellite measurements and the model output can be neglected. Figure A2 (a) shows profiles of NO_2 concentration for the regions ANE and ASE for four months. Apparently, NO_2 is located at higher altitudes in ASE, which leads to differences in the visibility of the NO_2 signal between the two spectral ranges. This is partly related to the surface altitude which is on average ~ 830 m above sea level in ASE and only ~ 440 m in ANE. This could explain why the UV fit shows enhanced NO_2 over ASE and not over ANE.

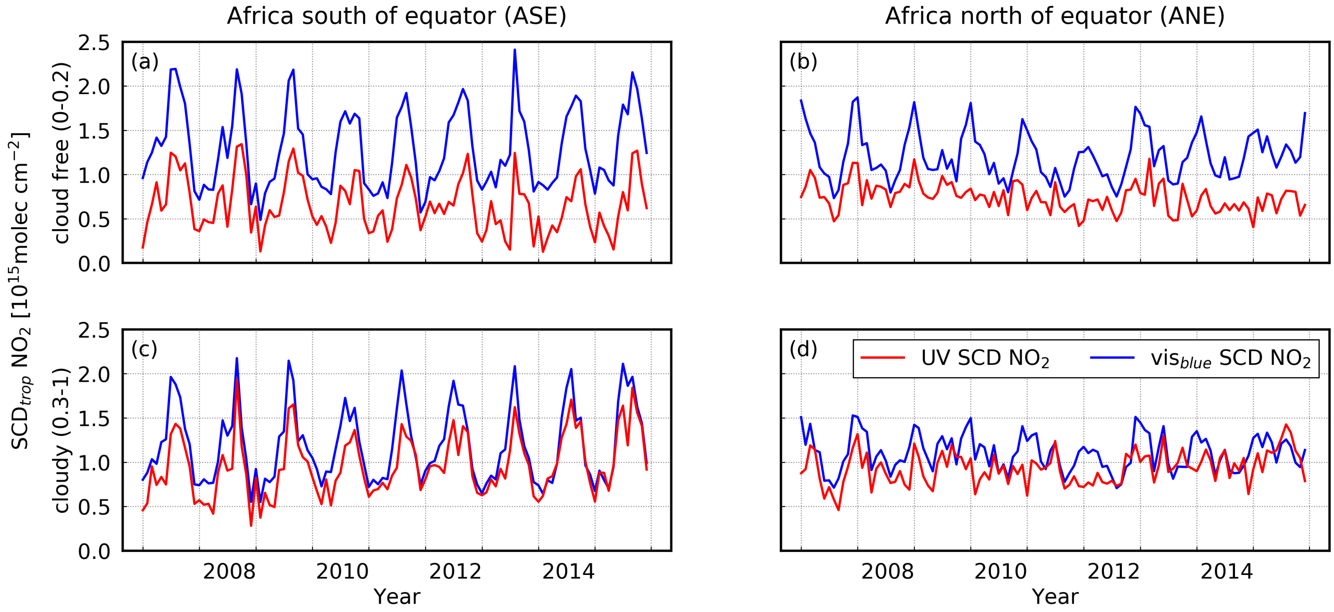

Figure A1. Tropospheric NO_2 SCD time series for ASE (a, c) and ANE (b, d) for cloud free scenes ($\leq 20\,\%$ cloud fraction; a, b) and for cloudy scenes ($\geq 30\,\%$ cloud fraction; c, d). The vertical lines indicate January of the individual years. (a, b) are identical to Fig. 11 a, b and are replicated here to facilitate direct comparison.

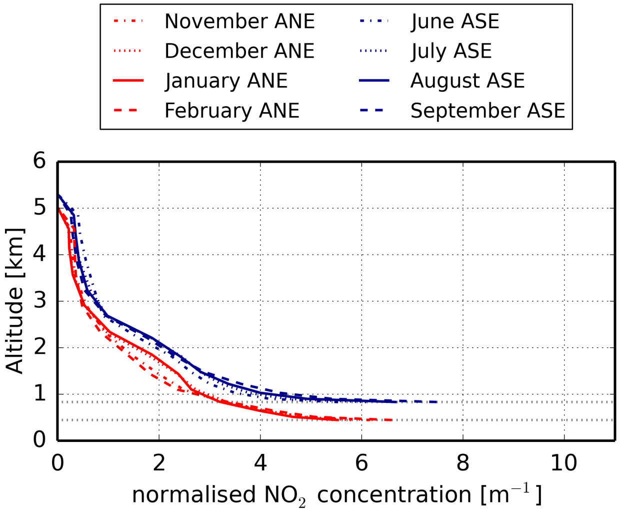

Figure A2. Average profiles of normalised NO_2 concentration for the three regions ANE and ASE for 2008, derived from the TM5-MP for 09:00 LT. The grey dashed lines indicating the surface height of the two regions.

A3 Seasonality of stratospheric NO_2

Figure A3 shows time series of detrended total SCDs for the regions ANE and ASE. Detrending is necessary because of the degradation of the instrument (Dikty and Richter, 2011), and is implemented as subtraction of a linear trend. Here, a shortened time series from 2008 to 2012 is used, since changes in the instrument configuration (EUMETSAT, 2015) might introduce an offset after 2012.

In ASE a clear seasonal cycle can be seen for both spectral ranges (Fig. A3 a), which agrees well with the seasonal cycle expected from biomass burning activity. However, comparison with Fig. A3 c shows that a similar seasonal cycle can also be observed in SCD data over the Pacific Ocean (averaged over $180°-210°$ E), which is void of any NO_x emissions and should therefore only have very low tropospheric NO_2 SCDs. This indicates that the seasonality over ASE is at least partly caused by stratospheric fluctuations.

Over ANE, slightly different seasonal cycles can be observed in the UV and blue spectral range (see Fig. A3 b). The peak related to biomass burning in NH winter is clearly observed in the vis_{blue} SCD data. In some years a small secondary peak in NH summer can be noticed. Similar seasonal variability can be seen in the UV spectral range, but both peaks have similar magnitude there. This double peak structure can also be found in NO_2 SCDs from the Ozone Monitoring Instrument (OMI, not shown). Over the Pacific Ocean (Fig. A3 d), the second peak in NH summer can clearly be observed in the UV data, corresponding to the known seasonal variability of stratospheric NO_2. As the seasonal cycles of biomass burning and stratospheric NO_2 are in-phase and out-of-phase for ASE and ANE, respectively, the visibility of the biomass burning NO_2 differs strongly between the two regions.

A4 Aerosol effect

The Cloud-Aerosol Lidar and Infrared Pathfinder Satellite Observations (CALIPSO) satellite is in a sun-synchronous polar orbit with an equator crossing time of 13:30 LT (Winker et al., 2007). It was launched in April 2006 and has a repeat cycle of 16 days. On CALIPSO, the Cloud-Aerosol Lidar with Orthogonal Polarisation (CALIOP) instrument is operating since June 2006. CALIOP is a nadir-viewing two wavelength polarization-sensitive lidar, operating at 532 nm and 1064 nm. The horizontal and vertical resolution depends on the altitude. Closer to the ground the resolution increases in both cases (Winker et al., 2007; Winker et al., 2009).

Here, the CALIOP level 3 product “Aerosol Profile All Sky (daytime)” was used. The data are on a 2° latitude times 5° longitude grid (Atmosheric Science Data Center, 2009). For the calculation of regional aerosol contribution for smaller regions, the amount of aerosols in the grid box was weighted by the contribution of the grid box to the region. This dataset provides the six aerosol types “dust”, “polluted continental”, “smoke”, “clean marine”, “clean continental”, and “polluted dust”, where the latter accounts for a mixture of dust and smoke or a mixture of dust and urban pollution (Omar et al., 2009). The aerosol-types were derived using aerosol models based on cluster analysis of an AERONET dataset and the aerosol extinction-to-backscatter ratio (Omar et al., 2009). In the present study, the differences in equator crossing time can be ignored, because especially for ASE and ANE larger areas are averaged.

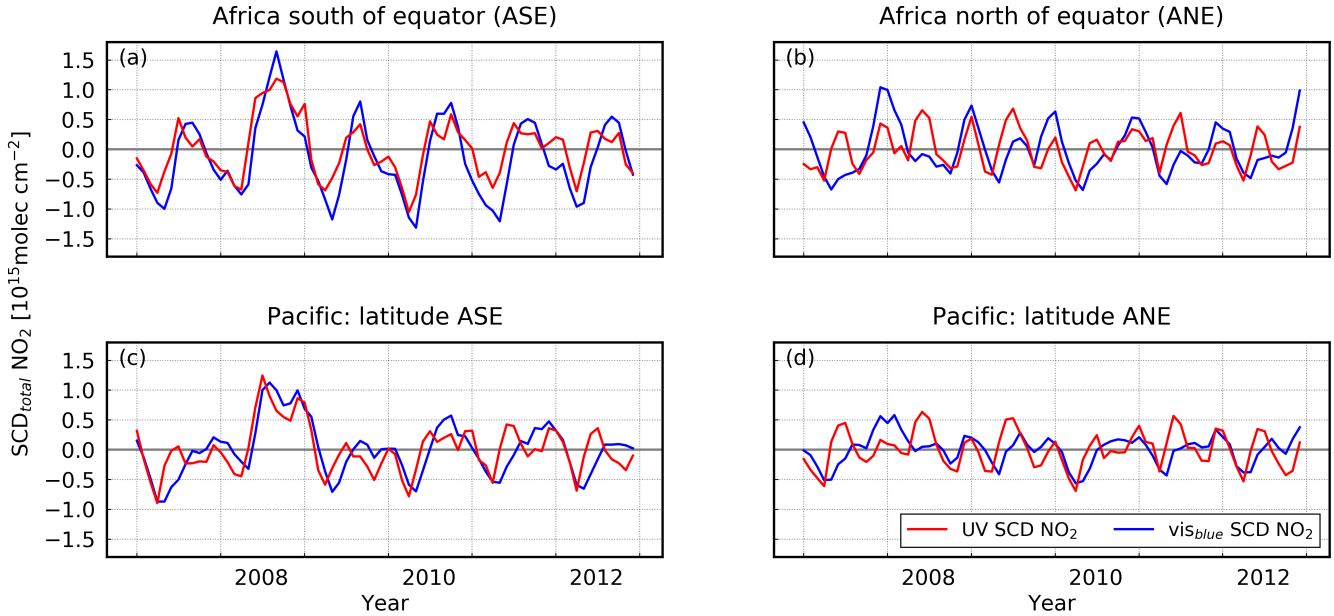

Figure A3. Time series of detrended total NO_2 SCDs for the UV and blue spectral range for ASE (a) and ANE (b) as well as detrended time series over the Pacific reference sector area for the latitude of ASE (c) and ANE (d). The vertical lines indicate January of the individual years.

Figure A4 shows the sample number for the six aerosol types over the three regions ANE, ASE, and Riyadh. The dominant aerosol-type in ASE is smoke whereas dust dominates in ANE and Riyadh.

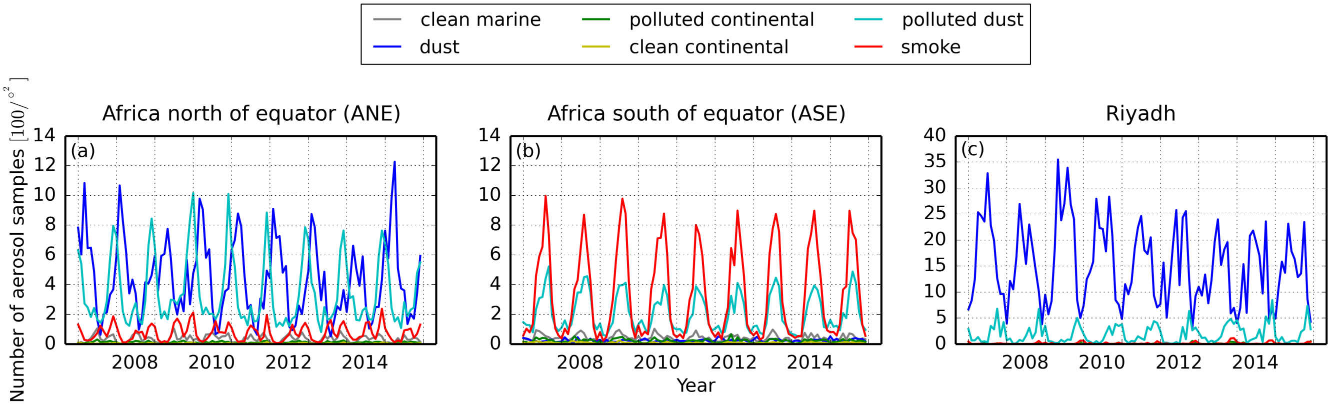

Figure A4. Time series for the number of samples of aerosol-types for three different regions (CALIPSO data). To calculate the time series for the individual areas, the amount of aerosol in the grid box was weighted by the contribution of the grid box to the region. Note the different y-axes. The vertical lines indicate January of the individual years.

Acknowledgements. This study has been funded by the EU FP7 project PArtnership with ChiNa on space DAta (PANDA, grant no. 606719), by DLR in the scope of the Sentinel-5 Precursor verification project (grant no. 50EE1247), by the University of Bremen, and the state of Bremen. GOME-2 lv1b radiances have been provided by EUMETSAT. The CALIOP data were obtained from the NASA Langley Research Center Atmospheric Science Data Center.

References

Archer-Nicholls, S., Lowe, D., Darbyshire, E., Morgan, W. T., Bela, M. M., Pereira, G., Trembath, J., Kaiser, J. W., Longo, K. M., Freitas, S. R., Coe, H., and McFiggans, G.: Characterising Brazilian biomass burning emissions using WRF-Chem with MOSAIC sectional aerosol, Geoscientific Model Development, 8, 549–577, doi:10.5194/gmd-8-549-2015, 2015.

Atmosheric Science Data Center: CALIPSO Quality Statements Lidar Level 3 Aerosol Profile Monthly Products Version Release: 1.00, Atmosheric Science Data Center, 2009.

Beirle, S., Platt, U., Wenig, M., and Wagner, T.: NOx production by lightning estimated with GOME, Advances in Space Research, 34, 793–797, doi:10.1016/j.asr.2003.07.069, 2004.

Belmonte Rivas, M., Veefkind, P., Eskes, H., and Levelt, P.: OMI tropospheric NO2 profiles from cloud slicing: Constraints on surface emissions, convective transport and lightning NOx, Atmospheric Chemistry and Physics, 15, 13 519–13 553, doi:10.5194/acp-15-13519-2015, 2015.

Bergstrom, R. W., Pilewskie, P., Russell, P. B., Redemann, J., Bond, T. C., Quinn, P. K., and Sierau, B.: Spectral absorption properties of atmospheric aerosols, Atmospheric Chemistry and Physics, 7, 5937–5943, doi:10.5194/acp-7-5937-2007, 2007.

Bertram, T. H., Heckel, A., Richter, A., Burrows, J. P., and Cohen, R. C.: Satellite measurements of daily variations in soil NOx emissions, Geophysical Research Letters, 32, doi:10.1029/2005GL024640, 2005.

Boersma, K. F., Eskes, H. J., and Brinksma, E.: Error analysis for tropospheric NO2 retrieval from space, Journal of Geophysical Research, 109, D04 311, doi:10.1029/2003JD003962, 2004.

Burrows, J. P., Weber, M., Buchwitz, M., Rozanov, V., Ladstätter-Weißenmayer, A., Richter, A., DeBeek, R., Hoogen, R., Bramstedt, K., Eichmann, K.-U., and Eisinger, M.: The Global Ozone Monitoring Experiment (GOME): Mission, instrument concept, and first scientific results, Journal of Atmospheric Sciences, 56, 151–175, doi:10.1175/1520-0469, 1999.

Burrows, J. P., Platt, U., and Borrell, P., eds.: The Remote Sensing of Tropospheric Composition from Space, Physics of Earth and Space Environments, Springer-Verlag Berlin Heidelberg, doi:10.1007/978-3-642-14791-3, 2011.

Callies, J., Corpaccioli, E., Eisinger, M., Hahne, A., and Lefebvre, A.: GOME-2 - Metop's second-generation sensor for operational ozone monitoring, ESA Bulletin-European Space Agency, 102, 28–36, 2000.

Chance, K., Burrows, J., Perner, D., and Schneider, W.: Satellite measurements of atmospheric ozone profiles, including tropospheric ozone, from ultraviolet/visible measurements in the nadir geometry: a potential method to retrieve tropospheric ozone, Journal of Quantitative Spectroscopy and Radiative Transfer, 57, 467–476, doi:10.1016/S0022-4073(96)00157-4, 1997.

Choi, S., Joiner, J., Choi, Y., Duncan, B. N., Vasilkov, A., Krotkov, N., and Bucsela, E.: First estimates of global free-tropospheric NO2 abundances derived using a cloud-slicing technique applied to satellite observations from the aura ozone monitoring instrument (OMI), Atmospheric Chemistry and Physics, 14, 10 565–10 588, doi:10.5194/acp-14-10565-2014, 2014.

Coheur, P.-F., Herbin, H., Clerbaux, C., Hurtmans, D., Wespes, C., Carleer, M., Turquety, S., Rinsland, C. P., Remedios, J., Hauglustaine, D., Boone, C. D., and Bernath, P. F.: ACE-FTS observation of a young biomass burning plume: first reported measurements of C2H4, C3H6O, H2CO and PAN by infrared occultation from space, Atmospheric Chemistry and Physics, 2, 5437–5446, doi:10.5194/acp-7-5437-2007, 2007.

Danielson, J. J. and Gesch, D. B.: Global Multi-resolution Terrain Elevation Data 2010 (GMTED2010), Tech. rep., U.S. Department of the Interior, U.S. Geological Survey, 2011.

Delon, C., Reeves, C. E., Stewart, D. J., Serc, D., Dupont, R., Mari, C., and Tulet, P.: Biogenic nitrogen oxide emissions from soils – impact on NOx and ozone overWest Africa during AMMA (African Monsoon Multidisciplinary Experiment): modelling study, Atmospheric Chemistry and Physics, 8, 2351–2363, doi:10.5194/acp-8-2351-2008, 2008.

Dieudonné, E., Ravetta, F., Pelon, J., Goutail, F., and Pommereau, J. P.: Linking NO2 surface concentration and integrated content in the urban developed atmospheric boundary layer, Geophysical Research Letters, 40, 1247–1251, doi:10.1002/grl.50242, 2013.

Dikty, S. and Richter, A.: GOME-2 on MetOp-A Support for Analysis of GOME-2 In-Orbit Degradation and Impacts on Level 2 Data Products Final Report, Tech. rep., University of Bremen, Institut of Remote Sensing, 2011.

Dirksen, R. J., Boersma, K. F., Eskes, H. J., Ionov, D. V., Bucsela, E. J., Levelt, P. F., and Kelder, H. M.: Evaluation of stratospheric NO2 retrieved from the Ozone Monitoring Instrument: Intercomparison, diurnal cycle, and trending, Journal of Geophysical Research: Atmospheres, 116, D08 305, doi:10.1029/2010JD014943, 2011.

Dubovik, O., Holben, B., Thomas, F. E., Smirnov, A., Kaufmann, Y. J., King, M. D., Tanré, D., and Slutsker, I.: Variability of Absorption and Optical Properties of Key Aerosol Types Observed in Worldwide Locations, American Meteorological Society, 59, 590–608, doi:10.1175/1520-0469(2002)059<0590:VOAAOP>2.0.CO;2, 2001.

EUMETSAT: GOME-2 Product Guide, Tech. Rep. v3, 2011.

EUMETSAT: GOME-2 Newsletter Archive, Tech. Rep. v4C, 2015.

Finlayson-Pitts, B. J. and Pitts, J. N.: Chemistry of the Upper and Lower Atmosphere: Theory, Experiments, and Applications, Acade, San Diego, 6 edn., doi:10.1002/bbpc.19860901231, 1999.

Gonzi, S. and Palmer, P. I.: Vertical transport of surface fire emissions observed from space, Journal of Geophysical Research Atmospheres, 115, 1–16, doi:10.1029/2009JD012053, 2010.

Greenblatt, G. D., Orlando, J. J., Burkholder, J. B., and Ravishankara, A. R.: Absorption measurements of oxygen between 330 and 1140 nm, Journal of Geophysical Research, 95, 18 577–18 582, doi:10.1029/JD095iD11p18577, 1990.

Gür, B., Spietz, P., Orphal, J., and Burrows, J. P.: Absorption Spectra Measurements with the GOME-2 FMs using the IUP/IFE-UB's Calibration Apparatus for Trace Gas Absorption Spectroscopy CATGAS, Tech. rep., IUP University of Bremen, doi:10.1017/CBO9781107415324.004, 2005.

Heue, K.-P., Richter, A., Wagner, T., Bruns, M., Burrows, J. P., v. Friedeburg, C., Lee, W. D., Platt, U., Pundt, I., and Wang, P.: Validation of SCIAMACHY tropospheric NO2-columns with AMAXDOAS measurements, Atmospheric Chemistry and Physics, 5, 1039–1051, doi:10.5194/acp-5-1039-2005, 2005.

Hilboll, A., Richter, A., and Burrows, J. P.: Long-term changes of tropospheric NO2 over megacities derived from multiple satellite instruments, Atmospheric Chemistry and Physics, 13, 4145–4169, doi:10.5194/acp-13-4145-2013, 2013a.

Hilboll, A., Richter, A., Rozanov, A., Hodnebrog, Ø., Heckel, A., Solberg, S., Stordal, F., and Burrows, J. P.: Improvements to the retrieval of tropospheric NO2 from satellite – stratospheric correction using SCIAMACHY limb/nadir matching and comparison to Oslo CTM2 simulations, Atmospheric Measurement Techniques, 6, 565–584, doi:10.5194/amt-6-565-2013, 2013b.

Hilboll, A., Richter, A., and Burrows, J. P.: Vertical information content of nadir measurements of tropospheric NO2 from satellite, in: Geophys. Res. Abstr., Vienna, Austria, doi:10.5281/zenodo.8746, http://meetingorganizer.copernicus.org/EGU2014/EGU2014-2882.pdf, 2014.

Hilboll, A., Richter, A., and Burrows, J. P.: NO2 pollution over India observed from space - the impact of rapid economic growth, and a recent decline, Atmospheric Chemistry and Physics Discussions, 20, doi:10.5194/acp-2017-101, 2017.

Huijnen, V., Williams, J., Van Weele, M., Van Noije, T., Krol, M., Dentener, F., Segers, A., Houweling, S., Peters, W., De Laat, J., Boersma, F., Bergamaschi, P., Van Velthoven, P., Le Sager, P., Eskes, H., Alkemade, F., Scheele, R., Nédélec, P., and Pätz, H. W.: The global chemistry transport model TM5: Description and evaluation of the tropospheric chemistry version 3.0, Geoscientific Model Development, 3, 445–473, doi:10.5194/gmd-3-445-2010, 2010.

Irie, H., Muto, T., Itahashi, S., Kurokawa, J.-i., and Uno, I.: Turnaround of Tropospheric Nitrogen Dioxide Pollution Trends in China, Japan, and South Korea, SOLA, 12, 170–174, doi:10.2151/sola.2016-035, 2016.

Jaeglé, L., Martin, R. V., Chance, K., Steinberger, L., Kurosu, T. P., Jacob, D. J., Modi, a. I., Yoboué, V., Sigha-Nkamdjou, L., and Galy-Lacaux, C.: Satellite mapping of rain-induced nitric oxide emissions from soils, Journal of Geophysical Research, 109, doi:10.1029/2004JD004787, 2004.

Kleipool, Q. L., Dobber, M. R., de Haan, J. F., and Levelt, P. F.: Earth surface reflectance climatology from 3 years of OMI data, Journal of Geophysical Research Atmospheres, 113, doi:10.1029/2008JD010290, 2008.

Lee, D. S., Köhler, I., Grobler, E., Rohrer, F., Sausen, R., Gallardo-Klenner, L., Olivier, J. G. J., Dentener, F. J., and Bouwman, a. F.: Estimations of global NOx emissions and their uncertainties, Atmospheric Environment, 31, 1735–1749, doi:10.1016/S1352-2310(96)00327-5, 1997.

Lorente, A., Folkert Boersma, K., Yu, H., Dörner, S., Hilboll, A., Richter, A., Liu, M., Lamsal, L. N., Barkley, M., De Smedt, I., Van Roozendael, M., Wang, Y., Wagner, T., Beirle, S., Lin, J. T., Krotkov, N., Stammes, P., Wang, P., Eskes, H. J., and Krol, M.: Structural uncertainty in air mass factor calculation for NO2and HCHO satellite retrievals, Atmospheric Measurement Techniques, 10, 759–782, doi:10.5194/amt-10-759-2017, 2017.

Martin, R. V., Chance, K., Jacob, D. J., Kurosu, T. P., Spurr, R. J. D., Bucsela, E., Gleason, J. F., Palmer, P. I., Bey, I., Fiore, A. M., Li, Q., Yantosca, R. M., and Koelemeijer, R. B. a.: An improved retrieval of tropospheric nitrogen dioxide from GOME, Journal of Geophysical Research, 107(D20), 4437, doi:10.1029/2001JD001027, 2002.

Meller, R. and Moortgat, G. K.: Temperature dependence of the absorption cross sections of formaldehyde between 223 and 323 K in the wavelength range 225–375 nm, Journal of Geophysical Research, 105, 7089–7101, doi:10.1029/1999JD901074, 2000.

Munro, R., Klaes, D., Poli, G., Retscher, C., Lindstrot, R., Huckle, R., Lacan, A., Grzegorski, M., Holdak, A., Kokhanovsky, A., Livschitz, J., and Eisinger, M.: The GOME-2 instrument on the Metop series of satellites: instrument design, calibration, and level 1 data processing – an overview, Atmospheric Measurement Techniques, 9, 1279–1301, doi:10.5194/amt-9-1279-2016, 2016.

Noije, T. P. C. V., Eskes, H. J., Dentener, F. J., Stevenson, D. S., Ellingsen, K., Schultz, M. G., Wild, O., Amann, M., Atherton, C. S., Bergmann, D. J., Bey, I., Boersma, K. F., Butler, T., Cofala, J., Drevet, J., Fiore, A. M., Gauss, M., Hauglustaine, D. A., Horowitz, L. W., Isaksen, I. S. A., Krol, M. C., Pitari, G., Prather, M. J., Pyle, J. A., Lawrence, M. G., Martin, R. V., Montanaro, V., Richter, A., Rodriguez, J. M., Savage, N. H., Strahan, S. E., Sudo, K., Szopa, S., and Roozendael, M. V.: Multi-model ensemble simulations of tropospheric NO2 compared with GOME retrievals for the year 2000, Atmospheric Chemistry and Physics, 6, 2943–2979, doi:10.5194/acp-6-2943-2006, 2006.

Noxon, J. F.: Nitrogen Dioxide in the Stratosphere and Troposphere Measured by Ground-Based Absorption Spectroscopy, Science, 189, 547–549, doi:10.1126/science.189.4202.547, 1975.

Omar, A. H., Winker, D. M., Kittaka, C., Vaughan, M. A., Liu, Z., Hu, Y., Trepte, C. R., Rogers, R. R., Ferrare, R. A., Lee, K. P., Kuehn, R. E., and Hostetler, C. A.: The CALIPSO automated aerosol classification and lidar ratio selection algorithm, Journal of Atmospheric and Oceanic Technology, 26, 1994–2014, doi:10.1175/2009JTECHA1231.1, 2009.

Peters, E., Wittrock, F., Richter, A., and Burrows, J. P.: Formaldehyde and nitrogen dioxide over the remote western Pacific Ocean: SCIAMACHY and GOME-2 validation using ship-based MAX-DOAS observations, Atmospheric Chemistry and Physics, 12, 11 179–11 197, doi:10.5194/acp-12-11179-2012, 2012.

Platt, U. and Stutz, J.: Differential Optical Absorption Spectroscopy, Physics of Earth and Space Environments, Springer Berlin, doi:10.1007/978-3-540-75776-4, 2008.

Platt, U., Marquard, L., Wagner, T., and Perner, D.: Corrections for zenith scattered light DOAS, Geophysical Research Letters, 24, 1759–1762, doi:10.1029/97GL01693, 1997.

Puķīte, J., Kühl, S., Deutschmann, T., Platt, U., and Wagner, T.: Extending differential optical absorption spectroscopy for limb measurements in the UV, Atmospheric Measurement Techniques, 3, 631–653, doi:10.5194/amt-3-631-2010, 2010.

Richter, A.: Absorptionsspektroskopische Messungen stratosphärischer Spurengase über Bremen, 53°N, Ph.D. thesis, University of Bremen, 1997.

Richter, A. and Burrows, J. P.: Multi wavelength approach to the retrieval of tropospheric NO2 from GOME measurements, Tech. rep., Gothenburg, 2000.

Richter, A. and Burrows, J. P.: Tropospheric NO2 from GOME measurements, Advances in Space Research, 29, 1673–1683, doi:10.1016/S0273-1177(02)00100-X, 2002.

Richter, A., Eyring, V., Burrows, J. P., Bovensmann, H., Lauer, A., Sierk, B., and Crutzen, P. J.: Satellite measurements of NO2 from international shipping emissions, Geophysical Research Letters, 31, doi:10.1029/2004GL020822, 2004.

Richter, A., Burrows, J. P., Nüß, H., Granier, C., and Niemeier, U.: Increase in tropospheric nitrogen dioxide over China observed from space, Nature, 437, 129–132, doi:10.1038/nature04092, 2005.

Richter, A., Begoin, M., Hilboll, A., and Burrows, J. P.: An improved NO2 retrieval for the GOME-2 satellite instrument, Atmospheric Measurement Techniques, 4, 1147–1159, doi:10.5194/amt-4-1147-2011, 2011.

Richter, A., Hilboll, A., and Burrows, J. P.: Improving satellite retrievals of large tropospheric NO2 columns, in: EGU Abstr., pp. EGU2014–11 669, Vienna, Austria, 2014.

Richter, A., Hilboll, A., and Burrows, J. P.: Revisiting satellite derived tropospheric NO2 trends, in: Geophys. Res. Abstr., pp. EGU2015–10 674, Vienna, Austria, http://presentations.copernicus.org/EGU2015-10674_presentation.pdf, 2015.

Rio, C., Hourdin, F., and Chédin, A.: Numerical simulation of tropospheric injection of biomass burning products by pyrothermal plumes, Atmospheric Chemistry and Physics, 10, 3463–3478, doi:10.5194/acpd-9-18659-2009, 2010.

Rothman, L. S., Gordon, I. E., Barber, R. J., Dothe, H., Gamache, R. R., Goldman, A., Perevalov, V. I., Tashkun, S. A., and Tennyson, J.: HITEMP, the high-temperature molecular spectroscopic database, Journal of Quantitative Spectroscopy and Radiative Transfer, 111, 2139–2150, doi:10.1016/j.jqsrt.2010.05.001, 2010.

Rozanov, V., Rozanov, A., Kokhanovsky, A., and Burrows, J.: Radiative transfer through terrestrial atmosphere and ocean: Software package SCIATRAN, Journal of Quantitative Spectroscopy and Radiative Transfer, 133, 13–71, doi:10.1016/j.jqsrt.2013.07.004, 2014.

Russell, P. B., Bergstrom, R. W., Shinozuka, Y., Clarke, A. D., Decarlo, P. F., Jimenez, J. L., Redemann, J., Dubovik, O., and Strawa, A.: Absorption Angstrom Exponent in AERONET and related data as an indicator of aerosol composition, Atmospheric Chemistry and Physics, 10, 1155–1169, doi:10.5194/acp-10-1155-2010, 2010.

Schreier, S. F., Richter, A., Kaiser, J. W., and Burrows, J. P.: The empirical relationship between satellite-derived tropospheric NO2 and fire radiative power and possible implications for fire emission rates of NOx, Atmospheric Chemistry and Physics, 14, 2447–2466, doi:10.5194/acp-14-2447-2014, 2014.

Serdyuchenko, A., Gorshelev, V., Weber, M., Chehade, W., and Burrows, J. P.: High spectral resolution ozone absorption cross-sections – Part 2: Temperature dependence, Atmospheric Measurement Techniques, 7, 625–636, doi:10.5194/amt-7-625-2014, 2014.

Singer, S. F. and Wentworth, R. C.: Method for the determination of the vertical ozone distribution from a satellite, Journal of Geophyscal Research, 62, 299–308, doi:10.1029/JZ062i002p00299, 1957.

Stewart, D. J., Taylor, C. M., Reeves, C. E., and Mcquaid, J. B.: Biogenic nitrogen oxide emissions from soils: impact on NOx and ozone over west Africa during AMMA (African Monsoon Multidisciplinary Analysis): observational study, Atmospheric Chemistry and Physics, 8, 2285–2297, doi:10.5194/acp-8-2285-2008, 2008.

Stull, R. B.: An Introduction to Boundary Layer Meteorology, doi:10.5194/amt-7-4133-2014, 1988.

van der A, R. J., Eskes, H. J., Boersma, K. F., van Noije, T. P. C., Van Roozendael, M., De Smedt, I., Peters, D. H. M. U., and Meijer, E. W.: Trends, seasonal variability and dominant NOx source derived from a ten year record of NO2 measured from space, Journal of Geophysical Research: Atmospheres, 113, doi:10.1029/2007JD009021, 2008.

van der Werf, G., Randerson, J., Giglio, L., Collatz, J., Kasibhatla, P., Morton, D., and Defries, R.: The improved Global Fire Emissions Database (GFED) version 3: contribution of savanna, forest, deforestation, and peat fires to the global fire emissions budget, in: EGU General Assembly Conference Abstracts, vol. 12 of *EGU General Assembly Conference Abstracts*, p. 13010, 2010.

van Geffen, J. H. G. M., Boersma, K. F., Van Roozendael, M., Hendrick, F., Mahieu, E., De Smedt, I., Sneep, M., and Veefkind, J. P.: Improved spectral fitting of nitrogen dioxide from OMI in the 405–465 nm window, Atmospheric Measurement Techniques, 8, 1685–1699, doi:10.5194/amt-8-1685-2015, 2015.

von Engel, A. and Teixeira, J.: A Planetary Boundary Layer Height Climatology Derived from ECMWF Reanalysis Data, American Meteorological Society, pp. 6575–6590, doi:10.1175/JCLI-D-12-00385.1, 2013.

Vountas, M., Rozanov, V. V., and Burrows, J. P.: Ring effect: Impact of rotational Raman scattering on radiative transfer in earth’s atmosphere, Journal of Quantitative Spectroscopy and Radiative Transfer, 60, 943–961, doi:10.1016/S0022-4073(97)00186-6, 1998.

Wang, P., Richter, A., Bruns, M., Rozanov, V. V., Burrows, J. P., Heue, K.-P., Wagner, T., Pundt, I., and Platt, U.: Measurements of tropospheric NO2 with an airborne multi-axis DOAS instrument, Atmospheric Chemistry and Physics, 5, 337–343, doi:doi:10.5194/acp-5-337-2005, 2005.

Wang, P., Stammes, P., van der A, R., Pinardi, G., and van Roozendael, M.: FRESCO+: an improved O2 A-band cloud retrieval algorithm for tropospheric trace gas retrievals, Atmospheric Chemistry and Physics, 8, 6565–6576, doi:10.5194/acp-8-6565-2008, 2008.

Williams, E. J., Hutchinson, G. L., and Fehsenfeld, F. C.: NOx and N2O Emissions From Soil, Global Biogeochemical Cycles, 6, 351–388, doi:10.1029/92GB02124, 1992.

Williams, J. E., Boersma, K. F., Le Sager, P., and Verstraeten, W. W.: The high-resolution version of TM5-MP for optimised satellite retrievals: Description and Validation, Geoscientific Model Development, 10, 721–750, doi:10.5194/gmd-10-721-2017, 2017.

Wilmouth, D. M., Hanisco, T. F., Donahue, N. M., and Anderson, J. G.: Fourier Transform Ultraviolet Spectroscopy of the A 2Π3/2 ← X 2Π3/2 Transition of BrO, The Journal of Physical Chemistry A, 103, 8935–8945, doi:10.1021/jp991651o, 1999.

Winker, D. M., Hunt, W. H., and Mcgill, M. J.: Initial performance assessment of CALIOP, Geophysical Research Letters, 34, 1–5, doi:10.1029/2007GL030135, 2007.

Winker, D. M., Vaughan, M. A., Omar, A., Hu, Y., and Powell, K. A.: Overview of the CALIPSO Mission and CALIOP Data Processing Algorithms, Journal of Atmospheric and Oceanic Technology, 26, 2310–2323, doi:10.1175/2009JTECHA1281.1, 2009.

Wittrock, F., Oetjen, H., Richter, A., Fietkau, S., Medeke, T., Rozanov, A., and Burrows, J. P.: MAX-DOAS measurements of atmospheric trace gases in Ny-Ålesund - Radiative transfer studies and their application, Atmospheric Chemistry and Physics, 4, 955–966, doi:10.5194/acp-4-955-2004, 2004.

Yang, K., Carn, S. A., Ge, C., Wang, J., and Dickerson, R. R.: Advancing Measurements of Tropospheric NO2 from Space: New Algorithm and First Global Results from OMPS, Geophysical Research Letters, 41, 4777–4786, doi:10.1002/2014GL060136, 2014.

Zien, A. W., Richter, A., Hilboll, A., Blechschmidt, A. M., and Burrows, J. P.: Systematic analysis of tropospheric NO2 long-range transport events detected in GOME-2 satellite data, Atmospheric Chemistry and Physics, 14, 7367–7396, doi:10.5194/acp-14-7367-2014, 2014.

Zörner, J., Remmers, J., Dörner, S., Wang, Y., Eger, P., Pöhler, D., Behrendt, T., Meixner, F., Penning de Vries, M., and Wagner, T.: Nördlinger Ries campaign on Soil Emissions (NORISE) - DOAS measurements of NO2 and HCHO in an agricultural region, in: Geophys. Res. Abstr., pp. EGU2016–12 465–3, Vienna, Austria, http://meetingorganizer.copernicus.org/EGU2016/EGU2016-12465-3.pdf, 2016.